Dynamics and Robust Control of a Grid-Connected VSC in Multiterminal DC Grids Considering the Instantaneous Power of DC- and AC-Side Filters and DC Grid Uncertainty

Masoud Davari, *Student Member, IEEE*, and Yasser Abdel-Rady I. Mohamed, *Senior Member, IEEE*

***Abstract*—The electric energy sector is moving toward extensive integration of renewable and clean energy resources, energy storage units, and modern loads via highly efficient and flexible multiterminal dc grids integrated within the traditional ac grid infrastructure. A voltage-source converter (VSC) is the main technology enabling the interconnection of dc and ac grids. In such demanding applications, dc-link voltage control is crucial to maintain system stability. However, the dynamics and control of VSCs considering the instantaneous power of both ac- and dc-side filters and dc grid uncertainties are not addressed in the current literature. Furthermore, as shown in this paper, the uncertainty in the effective dc grid parameters, including filter capacitance and dc-side inductance owing to connecting/disconnecting electric devices to/from the dc grid remarkably affects the converter stability and performance. To overcome these difficulties, this paper presents 1) a detailed small-signal model of the dc-link dynamics in grid-connected VSCs considering the instantaneous power of both ac- and dc-side energy storage components, and 2) a robust optimal dc-link voltage controller. The proposed controller ensures excellent tracking performance, robust disturbance rejection, and robust performance against operating point and parameter variation with a simple fixed-parameter controller. A theoretical analysis, comparative simulation studies, and experimental results are presented to show the effectiveness of the proposed control structure.**

***Index Terms*—DC grids, dc-*LC* filter, dc-link voltage control, robust control, voltage-source converters (VSCs).**

I. Introduction

THE electric energy sector is moving toward extensive integration of renewable and clean energy resources, energy storage units, and modern loads via highly efficient and flexible multiterminal dc grids integrated within the traditional ac grid infrastructure. A voltage-source converter (VSC) is the main technology enabling the interconnection of dc and ac grids [1]–[19]. In either transmission or distribution networks, a grid-connected VSC is responsible for exchanging power between ac and dc networks. Indeed, dc-distributed energy resources, such as photovoltaic systems, directly connected wind farms, and solar implementations, along with many modern dc loads, such as data and communication centers, light-emitting diode-based lighting systems, motor drives, and electric or hybrid vehicles, can be connected to the dc side of a grid-connected VSC [9], [10].

Several aspects related to the dynamics and controls of VSCs, such as the current control, ac bus voltage control, dc-link voltage control, grid synchronization, and islanding detection, are addressed in the current literature [4]–[12]. However, some important aspects that directly affect the stability and performance of the dc-link voltage dynamics in grid-connected VSCs are not addressed. These issues are summarized as follows.

1) As the penetration level of dc grids increases in modern distribution and transmission networks, dc grid stability and power quality become crucial objectives. The use of a dc-side choke to reduce the input-line harmonics to meet the IEEE 519 limits, suppress voltage/current spikes, reduce ac ripple on the dc bus, reduce dv/dt and di/dt rates, solve nuisance tripping, and reduce dc bus transient overvoltages becomes essential in such demanding VSC applications [20]. Moreover, the dc-side energy storage components affect the instantaneous power flow in the converter, which in turns affects the dynamics of the dc-link voltage. Similarly, the instantaneous power of the ac-side filter affects the dc-link voltage small-signal dynamics by creating an operating point-dependent zero that changes the system dynamics from minimum phase to nonminimum phase in the rectification mode [12]. To the best of the authors' knowledge, modeling and analysis of grid-connected VSCs considering the instantaneous power of both ac- and dc-side energy storage components are not addressed in the current literature.
2) In dc and hybrid ac/dc grids, VSCs can be connected to different entities, such as dc sources and dc loads with their front-end filters and converters, on the dc side. The connection and disconnection of such devices with their frequency-dependent output impedances directly affect the performance and stability of the dc-link voltage dynamics of the interfacing VSC. For example, current source converters are interfaced to dc grids with an inductive dc filter (choke) [21], and advanced dc hub configurations connecting several renewable resources to dc grids [22] and Z-source converters are interfaced to dc grids

Manuscript received February 19, 2015; revised April 5, 2015; accepted May 3, 2015. Date of publication June 1, 2015; date of current version November 16, 2015. Recommended for publication by Associate Editor B. Wang.

The authors are with the Department of Electrical and Computer Engineering, University of Alberta, Edmonton, AB T6G 2V4, Canada (e-mail: davari@ualberta.ca; yasser_rady@ieee.org).

Color versions of one or more of the figures in this paper are available online at http://ieeexplore.ieee.org.

Digital Object Identifier 10.1109/TPEL.2015.2439645

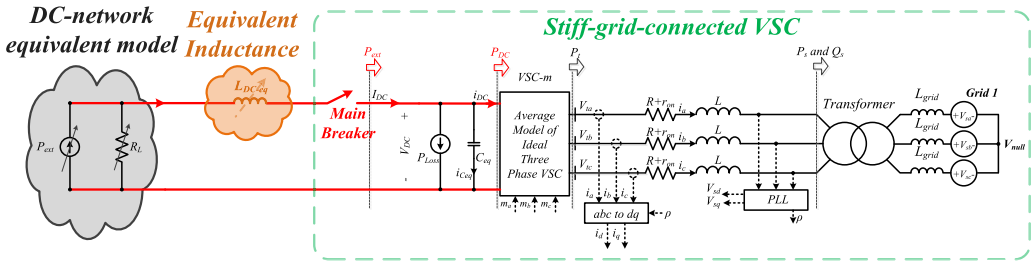

Fig. 1. Grid-connected VSC with equivalent dc network model.

via an *LC* network [23]. Therefore, the development of a robust dc-link voltage controller considering the impact of the energy storage components in the dc and ac sides and possible uncertainties demands special attention.

3) When the instantaneous power of both ac and dc energy storage components is considered, it can be shown that the dc-link voltage dynamics become highly dependent on the converter operation point (i.e., converter power or current levels, which vary in a wide negative to positive range owing to the bidirectional power nature of VSCs interfacing active dc grids to ac grids). Therefore, the dc-link voltage controller should be robust against operating point variation; i.e., to provide robust stability against equilibrium-to-equilibrium maneuver induced by operating point variation.

Motivated by the aforementioned difficulties, this paper presents a detailed small-signal model of a grid-connected VSC considering the impact of the instantaneous power of ac and dc filters on the dc-link voltage dynamics. A sensitivity study is conducted to gauge the impact of parametric uncertainty associated with energy storage components and operating point variation on the dc-link voltage dynamics. To ensure robust dc-link voltage control performance, a robust controller is synthesized considering possible uncertainties in the dc filter components. Furthermore, the controller is synthesized to yield robust performance and stability against equilibrium-to-equilibrium maneuver resulting from operating point variation [9], [10]. The controller is optimally synthesized using the μ-synthesis approach employing the *DK*-iteration algorithm owing to the fact that external active and reactive powers affect the dc-link voltage dynamics as exogenous disturbances. Therefore, by minimizing the H_∞ norm from exogenous disturbance to the output, which is the dc-link voltage, optimal disturbance rejection is achieved in the proposed controller. A theoretical analysis, comparative simulation studies, and experimental results are presented to show the effectiveness of the proposed control structure.

II. Modeling of a Grid-Connected VSC With DC-*LC* Filter

A typical 2.5-MW 580-V_{ac} 1500-V_{dc} 60-Hz grid-connected VSC for dc grid applications with uncertain dc inductor and ac-side inductive filter is shown in Fig. 1. The system parameters are given in Appendix I. In Fig. 1, $L_{\mathrm{DC-eq}}$ and C_{eq} are the equivalent inductance and capacitance, respectively, reflected to the dc side of the grid-connected VSC, and R_{res} is the filter damping resistor to suppress possible resonance in the *LC*-dc filter. Both $L_{\mathrm{DC-eq}}$ and C_{eq} are subjected to uncertainty in their nominal values, which is a practical assumption owing to the uncertainty associated with the operation of the dc grid and the connection and disconnection of dc generators and loads with their front-end converters and filters, which affect the equivalent values of $L_{\mathrm{DC-eq}}$ and C_{eq}. An *L*-based ac filter with equivalent inductance L (representing the summation of filter and transformer leakage) and equivalent resistance R, which is commonly used in high-power converters, is adopted. Furthermore, if high-order ac-side filters are adopted—e.g., *LC* or *LCL* filter—it has been found that their impact on the dc-link voltage dynamics is negligible owing to the frequency-scale separation between the *LCL* filter dynamics and dc-link voltage dynamics. In other words, the bandwidth of the dc-link voltage control loop is usually less than the fundamental frequency (in the range of 20 to 50 Hz); in this range, the ac-side filter behaves mainly as an *L* filter [24]. Therefore, the use of an *L* filter in this analysis is not a restricting assumption. The internal losses of the VSC are modeled by equivalent resistance r_{on} on the ac side and a current source on the dc side to model the power loss P_{loss} due to the reverse recovery and tailing current processes of the power switches. The dc grid is modeled by: 1) a variable current source representing external power P_{ext} that can be delivered or absorbed from the dc grid by dc generators and/or converter-based loads with regulated output power (i.e., active loads); and 2) an equivalent resistance R_{Load} representing equivalent passive loads in the dc grid. It should be noted that it is extremely difficult and impractical to design the converter control system based on the overall exact system dynamics, which contain both the dc and ac grid dynamics. Therefore, the equivalent models of both grids (i.e., a Thevenin's equivalent circuit model of the ac grids and Norton's equivalent circuit of the dc grid) are usually assumed during the analysis and control design stages [12]. A standard grid-oriented vector control scheme is adopted in this study owing to its widespread acceptance in the power converter industry. In this scheme, two proportional-integral (PI) current controllers (inner controllers) and an outer dc-link voltage controller are adopted. The dc-link voltage controller generates the *d*-axis reference current component, whereas the *q*-axis reference current component is set to zero to yield unit power factor operation. A standard *dq*-based three-phase phase-locked loop is adopted to extract the synchronization angle (ρ).

According to Fig. 1, an accurate model of the dc-link dynamics can be obtained when the total instantaneous power in the storage devices—i.e., $L_{\mathrm{DC-eq}}$ and C_{eq}—is considered. The

power balance across the dc-link capacitor can be given by

$$P_{\rm ext} - P_{\rm loss} - \frac{V_{\rm DC}^2}{R_L} - D\left(0.5L_{\rm DC-eq}I_{\rm DC}^2\right) - D(0.5C_{\rm eq}V_{\rm DC}^2) = P_{\rm DC} = P_t \quad (1)$$

where $V_{\rm DC}$ is the dc-link voltage; $I_{\rm DC}$ is the current flowing in the dc inductor; $C_{\rm eq}$ is the equivalent dc-link capacitance as seen from the VSC dc side, which includes the main dc-link capacitance and filter capacitance; $L_{\rm DC-eq}$ is the equivalent inductance of the dc inductor, which may vary from the nominal value due to uncertainties; $P_{\rm ext}$ is the external power injected to the dc side; $P_{\rm loss}$ is the power losses in the converter circuit; R_L is the equivalent static resistance reflected at the dc side of the VSC; $P_{\rm DC}$ is the net power as shown in Fig. 1, which is equal to the VSC ac-side terminal power P_t; and D is the time-derivative operator—i.e., $Dx = d(x)/dt$. It should be noted that P_t is not the same as the power injected into the grid (P_s), owing to the presence of the ac-side filter.

In (1), $V_{\rm DC}$ is considered to be the controlled output, whereas $P_{\rm DC}$ or P_t can be regarded as the input to this dynamic model. Therefore, the current $I_{\rm DC}$ should be expressed based on the output—i.e., either $V_{\rm DC}$ or $V_{\rm DC}^2$ and input signal $P_{\rm DC}$. Using Kirchhoff's current law, $I_{\rm DC}$ can be given by

$$\left.\begin{aligned} I_{\rm DC} &= i_{C\rm eq} + i_{\rm DC} \\ i_{C\rm eq} &= C_{\rm eq}DV_{\rm DC} \end{aligned}\right\} \Rightarrow DI_{\rm DC} = C_{\rm eq}D^2V_{\rm DC} + Di_{\rm DC} \quad (2)$$

where $i_{C\rm eq}$ is the current flowing into the capacitor of the dc filter, $i_{\rm DC}$ is the injected current into the dc side of the VSC after the equivalent capacitor $C_{\rm eq}$, and D^2 represents the second derivative over time—i.e., $D^2x = d^2x/dt^2$.

Using (2) into (1), the instantaneous power in $L_{\rm DC-eq}$ can be given by

$$\begin{aligned} 0.5L_{\rm DC}DI_{\rm DC}^2 = {} & L_{\rm DC-eq}C_{\rm eq}^2DV_{\rm DC}D^2V_{\rm DC} \\ & + L_{\rm DC-eq}C_{\rm eq}Di_{\rm DC}DV_{\rm DC} \\ & + L_{\rm DC-eq}C_{\rm eq}i_{\rm DC}D^2V_{\rm DC} \\ & + L_{\rm DC-eq}i_{\rm DC}Di_{\rm DC} \end{aligned} \quad (3)$$

where $i_{\rm DC}$ can be expressed using $P_{\rm DC}$ and $V_{\rm DC}$ as $i_{\rm DC} = P_{\rm DC}/V_{\rm DC}$. Consequently

$$Di_{\rm DC} = \frac{V_{\rm DC}DP_{\rm DC} - P_{\rm DC}DV_{\rm DC}}{V_{\rm DC}^2}. \quad (4)$$

Now let $x_1 = V_{\rm DC}$ and $x_2 = DV_{\rm DC}$; using (1), (3), and (4), the following power balance equation can be obtained:

$$\begin{aligned} P_{\rm ext} - {} & P_{\rm loss} - \frac{x_1^2}{R_L} - L_{\rm DC-eq}C_{\rm eq}^2x_2Dx_2 \\ & - L_{\rm DC-eq}C_{\rm eq}\frac{x_2}{x_1}x_2DP_{\rm DC} + L_{\rm DC-eq}C_{\rm eq}\frac{x_2^2}{x_1^2}P_{\rm DC} \\ & - L_{\rm DC-eq}C_{\rm eq}\frac{P_{\rm DC}}{x_1}Dx_2 - L_{\rm DC-eq}\frac{P_{\rm DC}}{x_1^2}DP_{\rm DC} \\ & + L_{\rm DC-eq}\frac{x_2}{x_1^3}P_{\rm DC}^2 - C_{\rm eq}x_1x_2 - P_{\rm DC} \\ = {} & F(x_1, x_2, Dx_2, P_{\rm DC}, DP_{\rm DC}, P_{\rm ext}, P_{\rm loss}) = 0. \end{aligned} \quad (5)$$

The nonlinear dynamics in (5) can be linearized using the Taylor series expansion on the dynamic function F around one equilibrium point (E.P.) as given by

$$\begin{aligned} & F(x_1, x_2, Dx_2, P_{\rm DC}, DP_{\rm DC}, P_{\rm ext}, P_{\rm loss}) \\ & = F|_{(\rm E.P.)} + \frac{\partial F}{\partial P_{\rm ext}}|_{(\rm E.P.)}\tilde{P}_{\rm ext} + \frac{\partial F}{\partial P_{\rm loss}}|_{(\rm E.P.)}\tilde{P}_{\rm loss} \\ & + \frac{\partial F}{\partial x_1}|_{(\rm E.P.)}\tilde{x}_1 + \frac{\partial F}{\partial x_2}|_{(\rm E.P.)}\tilde{x}_2 + \frac{\partial F}{\partial (Dx_2)}|_{(\rm E.P.)}\tilde{D}x_2 \\ & + \frac{\partial F}{\partial P_{\rm DC}}|_{(\rm E.P.)}\tilde{P}_{\rm DC} + \frac{\partial F}{\partial (DP_{\rm DC})}|_{(\rm E.P.)}\tilde{D}P_{\rm DC} + \{\rm H.O.T.\} \end{aligned} \quad (6)$$

where $\sim$ indicates the perturbed signal around the E.P. of each variable, and high-order terms (H.O.T.) are ignored in order to linearize (6). Furthermore, the E.P. can be expressed by (7) considering that all variables are static at the equilibrium state

$$\begin{aligned} (\rm E.P.) &= (x_{1-0}, x_{2-0}, Dx_{2-0}P_{\rm DC-0}, DP_{\rm DC-0}, P_{\rm ext-0}, P_{\rm loss-0}) \\ &= (V_{\rm DC-nominal}, 0, 0, P_{\rm DC-0}, 0, P_{\rm ext-0}, P_{\rm loss-0}) \end{aligned} \quad (7)$$

where subscript "0" denotes the value of the variable at the E.P.

After mathematical manipulation, the linearized small-signal dynamics of (5) can be given by

$$\begin{aligned} \tilde{P}_{\rm ext} - {} & \tilde{P}_{\rm loss} - \tilde{P}_{\rm DC} - L_{\rm DC-eq}C_{\rm eq}\frac{P_{\rm DC-0}}{V_{\rm DC-nominal}}\tilde{D}x_2 \\ & - L_{\rm DC-eq}\frac{P_{\rm DC-0}}{V_{\rm DC-nominal}^2}\tilde{D}P_{\rm DC} + L_{\rm DC-eq}\frac{P_{\rm DC-0}^2}{V_{\rm DC-nominal}^3}\tilde{x}_2 \\ & - C_{\rm eq}V_{\rm DC-nominal}\tilde{x}_2 - \frac{2V_{\rm DC-nominal}}{R_p}\tilde{x}_1 = 0. \end{aligned} \quad (8)$$

Equation (8) reveals that the relationship must be found between $P_{\rm DC}$ and the main control input (lever) $I_{\rm d}$—i.e., the d-component of the ac current injected or absorbed from the ac grid—in order to reach a linear time-invariant (LTI) model describing the relationship between the output $V_{\rm DC}$ and the control input I_d. A similar process should be applied to $D\tilde{P}_{\rm DC}$ as shown in (8). In this regard, considering the total power balance on the ac side is essential to account for the effect of the instantaneous power of the ac-side filter as well. Equation (9) describes this power balance as follows:

$$P_{\rm DC} = P_t = P_{\rm loss\_R} + P_{\rm filter\_L} + P_s \quad (9)$$

where $P_{\rm loss\_R}$ is the total instantaneous power loss in the equivalent resistance of the inductor L, $P_{\rm loss\_L}$ is the total instantaneous power of the ac-side inductor L, and P_s is the total instantaneous power that must be absorbed/injected from/to the point of common coupling (PCC) in order to stabilize the dc-link voltage.

Owing to the fact that a standard vector-current-controlled-based VSC is employed as the actuator of active and reactive powers at the PCC, all equations should be expressed based on current components in the synchronous dq-frame, which is the most common framework for analysis and control of power converters [11]. Hence, all terms of (2) should be expressed using the dq-components of the current space vector $\vec{I}$, which has active and reactive components I_d and I_q. To start this

conversion process, the total instantaneous power absorbed by a three-wire three-phase network can be expressed by

$$P_{3-\text{wire}\,3-\text{phase network}} = \text{Re}\left\{1.5\vec{v}(t)\vec{i}^{*}(t)\right\} \tag{10}$$

where $\vec{v}$ and $\vec{i}$ represent the space vectors of the applied voltage and feeding current, respectively, into the three-wire three-phase network. Using (10), the following equations can be reached for all terms of (9)

$$\begin{aligned} P_{\text{loss\_}R} &= \text{Re}\left\{1.5\vec{v}_R(t)\vec{i}_R^{*}(t)\right\} = \text{Re}\left\{1.5R\vec{I}(t)\vec{I}^{*}(t)\right\} \\ &= 1.5R\,|I|^2 = 1.5R((I_d)^2+(I_q)^2) \end{aligned} \tag{11}$$

where I_d and I_q are the *dq* components of the VSC output current, and *R* is the equivalent filter resistance.

The total stored energy in the three-phase inductor *L* is expressed by

$$W_L = 0.5L(i_a^2+i_b^2+i_c^2) \tag{12}$$

where i_a, i_b, and i_c are the three-phase currents injected into the three-phase inductor *L*; they are assumed to be in the form of (13) at one general operating point

$$\begin{cases} i_a^2 = I^2\cos^2(\omega t-\varphi_i) \\ i_b^2 = I^2\cos^2\left(\omega t-\varphi_i-\dfrac{2\pi}{3}\right) \Rightarrow i_a^2+i_b^2+i_c^2 = 1.5I^2 \\ i_c^2 = I^2\cos^2\left(\omega t-\varphi_i-\dfrac{4\pi}{3}\right) \end{cases} \tag{13}$$

where *I* and φ are the amplitude and phase of the space vector $\overrightarrow{I}$, respectively. Consequently, (14) is reached for the instantaneous power of the three-phase inductor *L*

$$P_{\text{filter\_}L} = 0.75LD((I_d)^2+(I_q)^2). \tag{14}$$

Under unity power factor operation (i.e., $I_q=0$) and/or perfect synchronization (i.e., $V_q=0$), P_s can be given by

$$P_s = 1.5I_dV_{d_s} \tag{15}$$

where V_{d_s} is the *d*-component of the voltage space vector at the PCC.

Using (9)–(15), the relationship between P_{DC}, I_d, and the other signals, which are treated as disturbances, can be given by

$$\begin{aligned} &P_{\text{DC}} - 0.75LD(I_d)^2 - 1.5R(I_d)^2 - 1.5I_dV_{d_s} - 0.75LD(I_q)^2 \\ &\quad - 1.5R(I_q)^2 = G(I_d, DI_d, I_q, DI_q) = 0. \end{aligned} \tag{16}$$

Consequently, (16) can be used into (8) to find perturbed signal $\tilde{P}_{\text{DC}}$.

Again, because of the fact that (16) is a nonlinear equation, it is possible to employ the Taylor series expansion on the dynamic function *G* around one E.P. as follows:

$$\begin{aligned} G(I_d, DI_d, I_q, DI_q) = {} & G|_{(\text{E.P.})} + \frac{\partial G}{\partial I_d}|_{(\text{E.P.})}\tilde{I}_d \\ & + \frac{\partial G}{\partial DI_d}|_{(\text{E.P.})}\tilde{D}I_d + G|_{(\text{E.P.})} \\ & + \frac{\partial G}{\partial I_d}|_{(\text{E.P.})}\tilde{I}_q + \frac{\partial G}{\partial DI_q}|_{(\text{E.P.})}\tilde{D}I_q \\ & + \{\text{H.O.T.}\}. \end{aligned} \tag{17}$$

The E.P. of (16) can be expressed by

$$\begin{aligned} (\text{E.P.}) &= (I_{d-0}, DI_{d-0}, I_{q-0}, DI_{q-0}) \\ &= (I_{d-0}, 0, I_{q-0}, 0). \end{aligned} \tag{18}$$

After mathematical manipulation, (19) can be reached. It should be noted that all terms related to $\tilde{I}_q$ and $\tilde{D}I_q$ are lumped into the function g ($\tilde{I}_q$,$\tilde{D}I_q$), as shown in (19), owing to the fact that these signals are treated, in control terminology, as disturbance signals affecting the output signal. From the physical point of view, the dc-link energy, and hence the output V_{DC}, are mainly affected by active current component I_d

$$\begin{aligned} \tilde{P}_{\text{DC}} = {} & 1.5LI_{d-0}\tilde{D}I_d + 3RI_{d-0}\tilde{I}_d \\ & + 1.5V_{d_s}\tilde{I}_d + g(\tilde{I}_q, \tilde{D}I_q). \end{aligned} \tag{19}$$

In addition to (19), $D\tilde{P}_{\text{DC}}$ is also required to find the explicit transfer function between I_d and V_{DC} using (8). Using (16), DP_{DC} and its E.P. can be given by

$$\begin{aligned} DP_{\text{DC}} - {} & 1.5L(DI_d)^2 - 1.5LI_dD^2I_d - 3RI_dDI_d \\ & - 1.5V_{d_s}DI_d - 1.5L(DI_q)^2 - 1.5LI_dD^2I_q - 3RI_dDI_q \\ = {} & H(I_d, DI_d, D^2I_d, I_q, DI_q, D^2I_q) = 0 \end{aligned} \tag{20}$$

$$\begin{aligned} (\text{E.P.}) &= (I_{d-0}, DI_{d-0}, D^2I_{d-0}, I_{q-0}, DI_{q-0}, D^2I_{q-0}) \\ &= (I_{d-0}, 0, 0, I_{q-0}, 0, 0). \end{aligned} \tag{21}$$

Using the Taylor series expansion on the dynamic function *H* in (20), $\widetilde{DP_{\text{DC}}}$ can be given by

$$\begin{aligned} D\tilde{P}_{\text{DC}} = {} & 1.5LI_{d-0}D^2\tilde{I}_d + 3RI_{d-0}D\tilde{I}_d + 1.5V_{d_s}D\tilde{I}_d \\ & + h(I_q, DI_q, D^2I_q). \end{aligned} \tag{22}$$

Equations (8), (19), and (22) are combined to reach the final transfer function describing the relationship between I_d and V_{DC} as

$$\begin{aligned} \tilde{V}_{\text{DC}} = {} & \frac{as^2+bs+e}{As^2+Bs+E}\tilde{I}_d - R\frac{\text{Dist}(\tilde{I}_q, s\tilde{I}_q.s^2\tilde{I}_q)}{As^2+Bs+E} \\ & - \frac{\tilde{P}_{\text{loss}}}{As^2+Bs+E} - \frac{\tilde{P}_{\text{ext}}}{As^2+Bs+E} \\ a \triangleq {} & -1.5L_{\text{DC-eq}}L\frac{P_{\text{DC}-0}I_{d-0}}{V_{\text{DC-nominal}}^2} \\ b \triangleq {} & -L_{\text{DC-eq}}\frac{P_{\text{DC}-0}}{V_{\text{DC-nominal}}^2}(3RI_{d-0}+1.5LI_{d-0}+1.5V_{sd}) \\ & - 1.5LI_{d-0} \\ e \triangleq {} & -3RI_{d-0} - 1.5V_{sd} \\ A \triangleq {} & L_{\text{DC-eq}}C_{\text{eq}}\frac{P_{\text{DC}-0}}{V_{\text{DC-nominal}}} \end{aligned}$$

$$B \triangleq \left(C_{\rm eq}V_{\rm DC-nominal} - L_{\rm DC-eq}\frac{P^2_{\rm DC-0}}{V^3_{\rm DC-nominal}}\right)$$
$$E \triangleq \left(\frac{2}{R_L}V_{\rm DC-nominal}\right) \quad (23)$$

where Dist is a linear function of the set $\{\tilde{I}_q,\ s\tilde{I}_q,\ s^2\tilde{I}_q\}$, and, according to (9)–(15), $P_{\rm DC-0} = 1.5(RI^2_{d-0} + RI^2_{q-0} + V_{sd}I_{d-0})$.

Furthermore, from (16), $P_{\rm DC-0}$ at the E.P. can be obtained from the corresponding current components (I_{d-0}, I_{q-0}) as

$$P_{\rm DC-0} = 1.5R(I_{d-0})^2 + 1.5I_{d-0}V_{d_s} + 1.5R(I_{q-0})^2. \quad (24)$$

Finally, (23) presents the linearized LTI model of the dc-link dynamics considering the instantaneous power of all energy storage devices in a VSC with *LC*-dc and *L*-ac filters.

To complete the model, the current control dynamics must be included. In vector-controlled VSCs, the current control is conducted in the *dq*-frame with feed-forward and decoupling terms. Therefore, the closed-loop current control dynamics can be represented by the following transfer function [12]

$$\mathrm{TF}_{\rm current} = \frac{1}{T_i s + 1} \quad (25)$$

where T_i is the time constant of the current controller.

Therefore, the overall transfer function between $\tilde{V}_{\rm DC}$ and $\tilde{I}_d$ can be given by

$$\begin{aligned}\tilde{V}_{\rm DC}(s) &= \frac{as^2+bs+e}{As^2+Bs+E}\times\frac{1}{T_i s+1}\tilde{I}_d(s)\\ &= \frac{as^2+bs+e}{AT_i s^3+(BT_i+A)s^2+(ET_i+B)s+E}\tilde{I}_d(s).\end{aligned} \quad (26)$$

For the sake of performance comparison, two additional small-signal models of the dc-link voltage dynamics are considered. The first model is a simplified and conventional one that completely ignores the impact of the instantaneous power of the ac and dc filter components. In this case, the dc-link voltage dynamics will be related to the control input by [12]

$$\tilde{V}^2_{\rm DC}(s) = -1.5V_{sd}\frac{1}{0.5C_{\rm eq}s}\times\frac{1}{T_i s+1}\tilde{I}_d(s). \quad (27)$$

In this idealized case, the dc-link voltage dynamics model is independent of the converter operating point without any possible nonminimum phase behavior.

In the second case, the instantaneous power of the ac filter is considered, whereas the impact of the dc filter is completely ignored. In this case, the dc-link voltage small-signal dynamics can be given by [9], [10], [12]

$$\begin{aligned}\tilde{V}^2_{\rm DC}(s) = &-1.5\frac{R_L L I_{d-0}s + R_L(V_{sd}+2RI_{d-0})}{0.5R_L C_{\rm eq}s+1}\\ &\times\frac{1}{T_i s+1}\tilde{I}_d(s).\end{aligned} \quad (28)$$

It should be noted that the output in (28) is $V^2_{\rm DC}$, and it is $V_{\rm DC}$ in (29). For the sake of comparing (28) to (26), (29) can be derived from (28) to achieve the same output signal in both (29) and (26)—i.e., $V_{\rm DC}$. Then

$$\begin{aligned}\tilde{V}_{\rm DC}(s) = &-1.5\frac{R_L L I_{d-0}s + R_L(V_{sd}+2RI_{d-0})}{R_L C_{\rm eq}V_{\rm DC-nominal}s + 2V_{\rm DC-nominal}}\\ &\times\frac{1}{T_i s+1}\tilde{I}_d(s).\end{aligned} \quad (29)$$

In either (28) or (29), it is clear that the magnitude of the linearized plant at an operating point is the same in both inversion and rectification modes; however, the phase is dramatically reduced at the same power in the rectification mode owing to the right-hand-plane (RHP) zero, which is generated in the rectification mode and affects the overall system stability and performance if the controller is designed based on the idealized model. Because (29) includes only the dynamics of the ac-side filter, (26) should converge to (29) if $L_{\rm DC-eq}$ is set to zero. If $L_{\rm DC-eq}$ is zero, (29) becomes a special case of (26); the values of *a*, *b*, *e*, *A*, *B*, and *E* are given in (30) for $L_{\rm DC-eq} = 0$

$$\begin{aligned}a &= 0\\ b &= -1.5LI_{d-0}\\ e &\triangleq -3RI_{d-0} - 1.5V_{sd}\\ A &= 0 \text{ then}\\ \tilde{V}_{\rm DC} &= \frac{-1.5LI_{d-0}s - 1.5V_{sd} - 3RI_{d-0}}{C_{\rm eq}V_{\rm DC-nominal}s + \frac{2}{R_L}V_{\rm DC-nominal}}\tilde{I}_d\\ &\quad - \text{Disturbance Signals.}\\ B &= C_{\rm eq}V_{\rm DC-nominal}\\ E &= \frac{2}{R_L}V_{\rm DC-nominal}\end{aligned} \quad (30)$$

Equation (26) shows that the dc-link voltage dynamics are remarkably different from the conventional simplified dynamics (27) when only the impact of the ac filter is considered (28). Equation (26) reveals that considering $L_{\rm DC}$ adds an additional zero and pole to the dynamics in (27); at different operating points and uncertainty in system parameters, the zero can lead to nonminimum phase dynamics, whereas the pole can be unstable. Physically, the impact of $L_{\rm DC}$ cannot be simply reflected to the ac side of the converter as an equivalent ac-side inductance to simplify the model. Similarly, the ac-side inductance *L* cannot be reflected to the dc side of the converter as an equivalent dc-side inductance. Indeed, both inductances and capacitances interact via the energy conversion process across the converter. The impact of different system parameters on the dynamic characteristics of (26) is discussed in the following section.

III. Discussion of DC-Link Dynamics of Grid-Connected VSC

The impact of different parameters on the stability and performance of the dc-link voltage dynamics is investigated here. This sensitivity study is important to identify the most critical system parameters and provide guidelines to design a robust dc-link voltage controller. The sensitivity study is conducted with respect to the dc-side filter parameters $L_{\rm DC-eq}$ and $C_{\rm eq}$ as

well as the power level of active and static loads on the dc grid represented by P_{ext} and R_L in Fig. 1, respectively.

A. Mathematical Analysis

Considering (26), one can mathematically analyze the location of the zeroes and poles of the linearized transfer function around one specific operating point using the Routh–Hurwitz criterion. Accordingly, the impact of different operating points as well as parameter variation on the location of the zeroes and poles can be quantified. If $T_i = 0$, the denominator of (26) becomes a second order polynomial, and the Routh-Hurwitz criterion is simplified as follows: if all coefficients *a*, *b*, and *e* have the same sign, then (26) does not have RHP zero. In addition, if all coefficients *A*, *B*, and *E* have the same sign, then (26) is stable.

1) Inversion Mode: First, suppose that the converter is operating in the inversion mode. Consequently, both $P_{\text{DC}-0}$ and *A* are positive, and, in order to have a stable transfer function in (26), *B* and *E* should be positive too. If only positive values of R_L (i.e., passive resistive dc-side load) are considered, *E* is always positive. Consequently, the value of *B* is important in the inversion mode; if (31a) is satisfied, then (26) is stable in the inversion mode, and if (31b) is satisfied, then (26) is unstable in the inversion mode

$$L_{\text{DC}-\text{eq}} < C_{\text{eq}} \frac{V^4_{\text{DC}-\text{nominal}}}{P^2_{\text{DC}-0}} \Rightarrow L_{\text{DC}-\text{eq}} < C_{\text{eq}} \frac{V^4_{\text{DC}-\text{nominal}}}{(1.5(RI^2_{d-0} + RI^2_{q-0} + V_{sd} I_{d-0}))^2} \quad (31a)$$

$$L_{\text{DC}-\text{eq}} > C_{\text{eq}} \frac{V^4_{\text{DC}-\text{nominal}}}{P^2_{\text{DC}-0}} \Rightarrow L_{\text{DC}-\text{eq}} > C_{\text{eq}} \frac{V^4_{\text{DC}-\text{nominal}}}{(1.5(RI^2_{d-0} + RI^2_{q-0} + V_{sd} I_{d-0}))^2}. \quad (31b)$$

Thus, since the maximum value of $P_{\text{DC}-0}$ is equal to the capacity of the converter ($\text{VSC}_{\text{Capacity}}$), (31) can be translated to (32) as a rule of thumb in the design procedure to achieve a stable system in the inversion mode

$$L_{\text{DC}-\text{eq}} < C_{\text{eq}} \frac{V^4_{\text{DC}-\text{nominal}}}{\text{VSC}^2_{\text{Capacity}}},$$

VSC is always stable in the inversion mode (32a)

$$L_{\text{DC}-\text{eq}} > C_{\text{eq}} \frac{V^4_{\text{DC}-\text{nominal}}}{\text{VSC}^2_{\text{Capacity}}},$$

VSC is always unstable in the inversion mode. (32b)

With regard to the location of zeroes, it is found out that the signs of *a*, *b*, and *e* are all negative because the signs of both $P_{\text{DC}-0}$ and I_{d-0} are the same provided that RI^2_{q-0} is negligible compared to $RI^2_{d-0} + V_{sd} I_{d-0}$, which is the case in all industrial and practical VSCs in order to achieve minimum losses associated with the series resistance of the inductive filter. Consequently, there will be no RHP zero in the inversion mode.

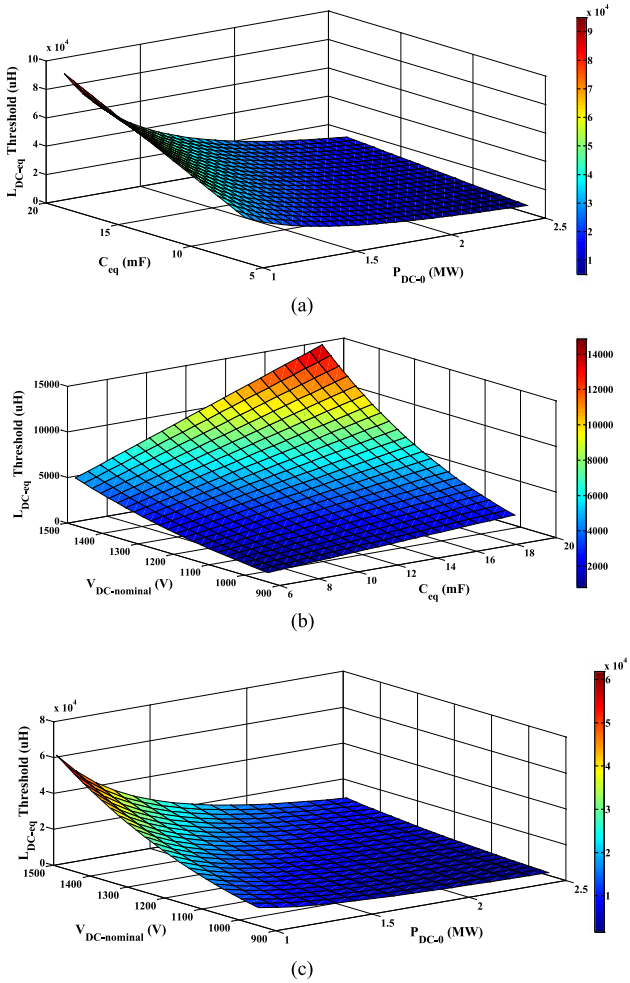

Fig. 2. Threshold value of $L_{\text{DC}-\text{eq}}$ for stable/unstable transfer function (26) in inversion/rectification mode; the effect of (a) $P_{\text{DC}-0}$ and C_{eq}, (b) $V_{\text{DC}-\text{nominal}}$ and C_{eq}, (c) $V_{\text{DC}-\text{nominal}}$ and $P_{\text{DC}-0}$.

2) Rectification Mode: Second, suppose that the converter is operating in the rectification mode. Consequently, $P_{\text{DC}-0}$ and *A* are negative; therefore, in order to have a stable transfer function in (26), *B* and *E* should be negative too. Again, if R_L is positive, *E* is always positive and (26) is unstable. Consequently, the value of *B* is important in the rectification mode; if (33a) is satisfied, then (26) is stable in the rectification mode, and if (33b) is satisfied, then (26) is unstable in the rectification mode

$$L_{\text{DC}-\text{eq}} > C_{\text{eq}} \frac{V^4_{\text{DC}-\text{nominal}}}{P^2_{\text{DC}-0}} \Rightarrow L_{\text{DC}-\text{eq}} > C_{\text{eq}} \frac{V^4_{\text{DC}-\text{nominal}}}{(1.5(RI^2_{d-0} + RI^2_{q-0} + V_{sd} I_{d-0}))^2} \quad (33a)$$

$$L_{\text{DC}-\text{eq}} < C_{\text{eq}} \frac{V^4_{\text{DC}-\text{nominal}}}{P^2_{\text{DC}-0}} \Rightarrow L_{\text{DC}-\text{eq}} < C_{\text{eq}} \frac{V^4_{\text{DC}-\text{nominal}}}{(1.5(RI^2_{d-0} + RI^2_{q-0} + V_{sd} I_{d-0}))^2}. \quad (33b)$$

Thus, since the maximum value of $P_{\text{DC}-0}$ is equal to the capacity of the converter, (33) can be translated to (34) as a rule

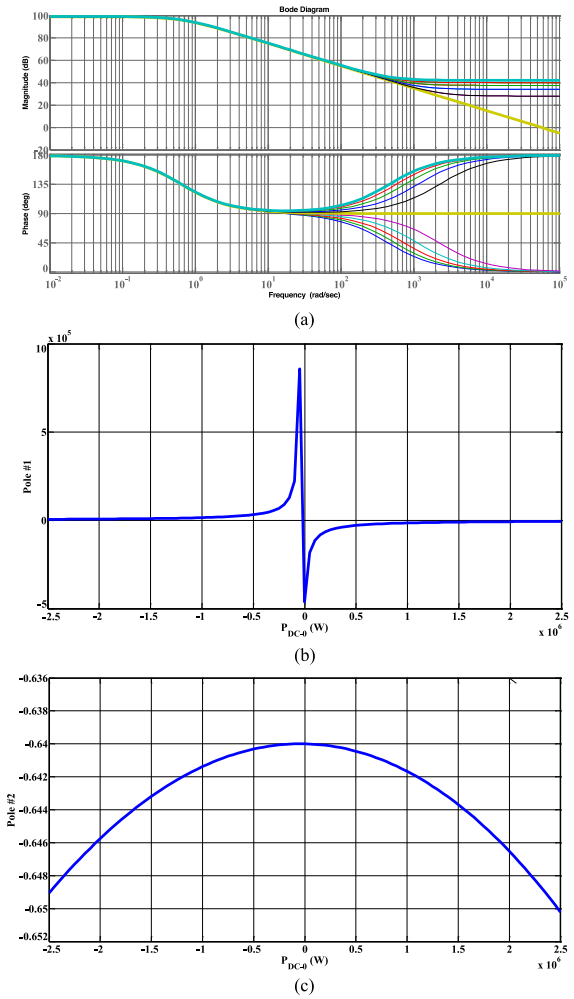

Fig. 3. (a) Frequency response of (26) for all operating pints from maximum rectification mode to the maximum inversion mode. (b) Effect of $P_{\mathrm{DC}-0}$ on the fast unstable pole, pole #2. (c) Effect of $P_{\mathrm{DC}-0}$ on the slow stable pole, pole #1.

TABLE I
POLES OF TRANSFER FUNCTION (26)

$P_{\mathrm{DC}-0}$ (MW)	$L_{\mathrm{DC}-\mathrm{eq}}$ (μH)	Pole #1	Pole #2
-2.5	150	6074.304	-0.649
-2.0	150	7636.865	-0.646
-1.5	150	10 252.624	-0.643
-1.0	150	15 554.333	-0.641
-0.5	150	32 160.057	-0.640
0.0	150	-461 346.775	-0.640
$+0.5$	150	-28 080.059	-0.640
$+1.0$	150	-14 417.290	-0.642
$+1.5$	150	-9658.104	-0.644
$+2.0$	150	-7231.582	-0.647
$+2.5$	150	-5756.041	-0.650

of thumb in the design procedure to achieve a stable system in the rectification mode

$$L_{\mathrm{DC}-\mathrm{eq}} > C_{\mathrm{eq}} \frac{V_{\mathrm{DC}-\mathrm{nominal}}^4}{\mathrm{VSC}_{\mathrm{Capacity}}^2}, \tag{34a}$$

VSC is always stable in the rectification mode

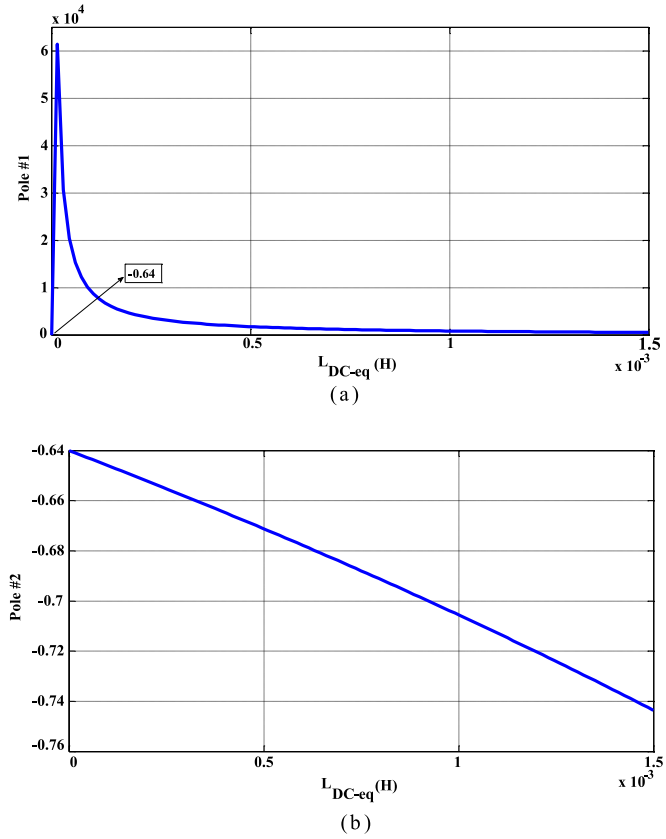

Fig. 4. Poles of (26) for changes in the value of $L_{\mathrm{DC}-\mathrm{eq}}$ from 0 to 1500 μH. (b) Effect of $L_{\mathrm{DC}-\mathrm{eq}}$ on the fast unstable pole, pole #2. (b) Effect of $L_{\mathrm{DC}-\mathrm{eq}}$ on the slow stable pole, pole #1.

TABLE II
POLES OF TRANSFER FUNCTION (26)

$P_{\mathrm{DC}-0}$ (MW)	$L_{\mathrm{DC}-\mathrm{eq}}$ (μH)	Pole #1	Pole #2
-2.5	0	-0.640	-0.640
-2.5	150	6074.304	-0.649
-2.5	300	2994.198	-0.658
-2.5	450	1967.502	-0.668
-2.5	600	1454.159	-0.678
-2.5	750	1146.158	-0.688
-2.5	900	940.827	-0.698
-2.5	1050	794.166	-0.709
-2.5	1200	684.172	-0.720
-2.5	1350	598.625	-0.732
-2.5	1500	530.190	-0.744

$$L_{\mathrm{DC}-\mathrm{eq}} < C_{\mathrm{eq}} \frac{V_{\mathrm{DC}-\mathrm{nominal}}^4}{\mathrm{VSC}_{\mathrm{Capacity}}^2}, \tag{34b}$$

VSC is always unstable in the rectification mode.

With regard to the location of zeroes, it is found out that the sign of a is always negative because of the fact that the signs of both $P_{\mathrm{DC}-0}$ and I_{d-0} are the same as discussed before. Consequently, the signs of b and e should also be negative to

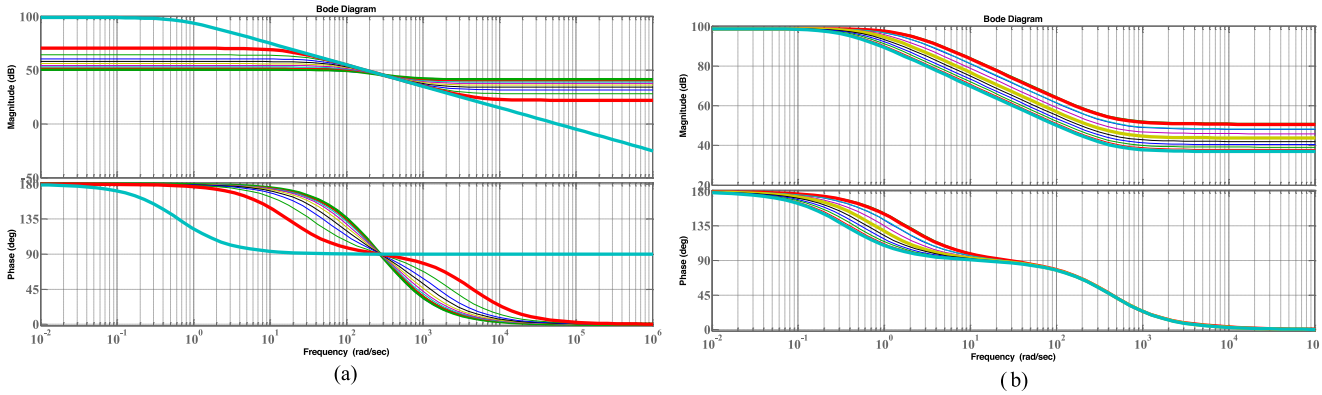

Fig. 5. (a) Frequency response of (26) for changes in the value of R_L from 0.903 to 250 Ω at $L_{\mathrm{DC-eq}} = 150$ μH. (b) Frequency response of (26) for changes in the value of C_{eq} from 6.250 to 22.509 mF at $R_{\mathrm{L}} = 250$ Ω.

prevent the creation of an RHP zero in the rectification mode. Equation (35) gives the conditions under which there will be no RHP zero in the rectification mode

$$\begin{cases} L_{\mathrm{DC-eq}} < \dfrac{1.5LI_{d-0}}{(3RI_{d-0} + 1.5LI_{d-0} + 1.5V_{sd})} \dfrac{V_{\mathrm{DC-nominal}}^2}{P_{\mathrm{DC-0}}} \\ \dfrac{-1.5V_{sd}}{3R + 1.5L} < I_{d-0} < 0 \end{cases}. \tag{35}$$

3) Threshold Point of Stability (Instability): As (31) and (33) reveal, there is one threshold value of $L_{\mathrm{DC-eq}}$ that makes the VSC stable/unstable depending on the VSC operating point, the nominal value of V_{DC} (i.e., $V_{\mathrm{DC-nominal}}$), and the value of C_{eq}; for that specific threshold value, a VSC is unstable either in rectification mode or inversion mode as (31) and (33) demonstrate. Fig. 2 shows the threshold value of $L_{\mathrm{DC-eq}}$ at different values of the VSC power at the rated values of $V_{\mathrm{DC-nominal}}$ and C_{eq}. A typical 2.5-MW 580-V_{ac} 1500-V_{dc} 60-Hz grid-connected VSC with parameters given in Appendix I [12] is used in the numerical analysis. It should be noted that $V_{\mathrm{DC-nominal}}$ is changing from the possible minimum value, $2V_{sd}$, to 1500 V, to show the effect of different possible nominal values of V_{DC} on the stability of the VSC. The obtained expressions provide useful guidelines to find the stability-related ranges of the dc-side inductance, which can vary in a wide range owing to system uncertainties.

4) Eigen Analysis and Frequency Responses: The frequency response of (26) is shown in Fig. 3 to illustrate the effect of different values of $P_{\mathrm{DC-0}}$ on the small-signal dynamics while $L_{\mathrm{DC-eq}}$ is fixed at 150 μH. The transfer function is unstable for some operating points; the poles related to each operating point along with $L_{\mathrm{DC-eq}} = 150$ μH are given in Table I. Moreover, the pole locations change when $P_{\mathrm{DC-0}}$ varies from the maximum rectification mode to the maximum inversion mode. Fig. 3(b) shows the trajectory of the fast pole, whereas Fig. 3(c) shows the trajectory of the slow pole when $P_{\mathrm{DC-0}}$ varies from the maximum rectification mode to the maximum inversion mode.

In addition, Fig. 4 shows the effect of different values of $L_{\mathrm{DC-eq}}$ on the poles of (26) when $P_{\mathrm{DC-0}}$ is fixed at –2.5 MW.

TABLE III
POLES OF TRANSFER FUNCTION (26)

R_L	$P_{\mathrm{DC-0}}$ (MW)	$L_{\mathrm{DC-eq}}$ (μH)	Pole #1	Pole #2
0.903	−2.50	150	6248.296	−174.641
1.004	−2.25	150	6925.338	−157.527
1.1300	−2.00	150	7776.507	−140.288
1.2923	−1.75	150	8877.899	−122.933
1.5090	−1.50	150	10 357.457	−105.476
1.8130	−1.25	150	12 448.203	−87.930
2.2704	−1.00	150	15 623.999	−70.308
3.0364	−0.75	150	21 019.145	−52.625
4.5824	−0.5	150	32 194.312	−34.895
9.3360	−0.25	150	69 082.434	−17.135
250	0	150	−461 346.775	−0.640

TABLE IV
POLES OF TRANSFER FUNCTION (26)

R_L	C_{eq} (F)	$P_{\mathrm{DC-0}}$ (MW)	$L_{\mathrm{DC-eq}}$ (μH)	Pole #1	Pole #2
250	0.006250	−2.5	150	5988.395	−1.3167
250	0.004375	−2.5	150	5914.774	−1.9044
250	0.004688	−2.5	150	5931.133	−1.7725
250	0.006093	−2.5	150	5983.989	−1.3514
250	0.008047	−2.5	150	6026.759	−1.0161
250	0.010273	−2.5	150	6055.683	−0.7921
250	0.012637	−2.5	150	6075.233	−0.6419
250	0.015068	−2.5	150	6088.949	−0.5371
250	0.017534	−2.5	150	6098.972	−0.4608
250	0.020017	−2.5	150	6106.570	−0.4031
250	0.022509	−2.5	150	6112.5101	−0.3581

It should be noted that the transfer function is unstable for all values of $L_{\mathrm{DC-eq}}$ as predicted from (33). The corresponding poles are given in Table II. The pole locations change when $L_{\mathrm{DC-eq}}$ varies from zero to the maximum value of 1500 μH, as shown in Fig. 4.

The values of R_L and C_{eq} dramatically affect the location of the poles/zeros of the small-signal dynamics in (26). Fig. 5 shows the frequency response of (26) due to change in R_L and C_{eq}; Tables III and IV reveal the location of poles for changes in R_L and C_{eq} as well.

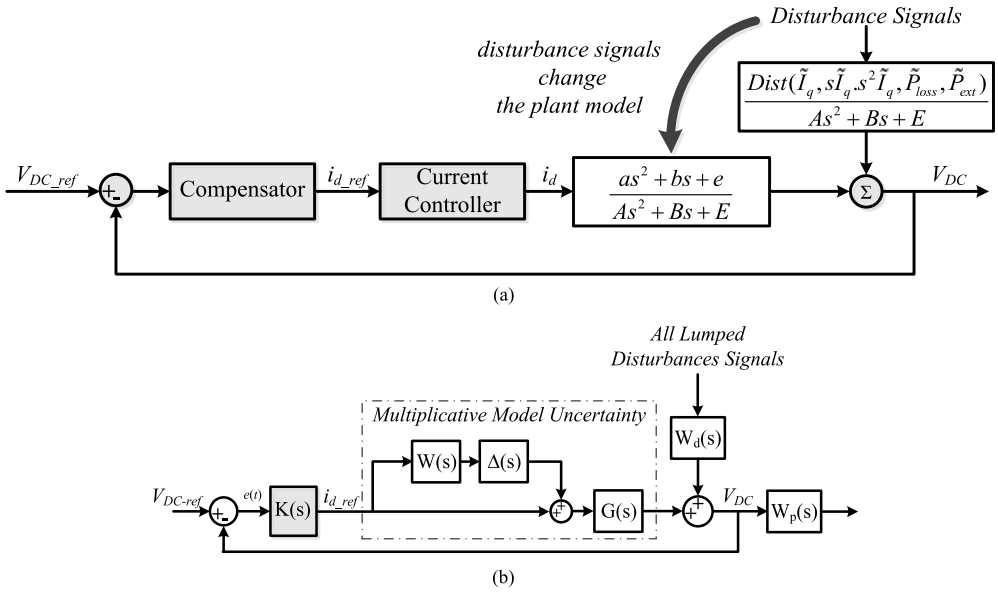

Fig. 6. (a) Proposed control scheme for a grid-connected VSC with uncertain dc-side *LC* filter. (b) Structure used to synthesize the feedback controller.

In fact, changes in R_L and $C_{\rm eq}$ change the slow dynamics of the nominal plant; however, $L_{\rm DC-eq}$ creates one unstable fast pole, provided that either (31) or (33) is satisfied for the criteria of instability in each mode of operation. An increase in $L_{\rm DC-eq}$ (i.e., due to unmodeled uncertainty) places the unstable pole close to the $j\omega$-axis from the RHP and makes it more dominant.

Owing to the fact that the open-loop plant is unstable in either the rectification mode or the inversion mode, the validity of the developed model is tested when the controller is synthesized for the linearized system, given by (26), and both the nonlinear dynamics and the linearized system are employed in the closed-loop system. The results of the nonlinear plant and linearized model with the same controller applied in the closed-loop system are then compared to validate the accuracy of the small-signal model. The validation results are provided in Section IV-B.

The results in Figs. 2–5 show that there are dramatic degradations in both the stability and the performance of the dc-side dynamics in a grid-connected VSC owing to the fact that all mentioned parameters can change the location of the poles and zeroes in a significant way. Consequently, not only operating point variation but also the parameters of the energy storage components within the converter system are able to degrade stability and performance. The situation becomes worse when parametric uncertainty is combined with operating point variation.

IV. Synthesizing a Robust Controller for Grid-Connected VSC With Uncertainty

According to the preceding analysis, because the nonminimum phase situation occurs along with unstable modes in the small-signal dynamics of (26), it is not possible to benefit from the robust control structure with two degree of freedom (DOF) proposed in [9] and [25], which requires a plant with stable poles. Furthermore, a switching adaptive controller [26] is not a suitable control candidate owing to the fact that both the operating point and the system parameters are changing, which yields a wide range of plant parameters and complicates the designd of a stable switching controller. Therefore, in this paper, an optimal robust controller that makes the closed-loop system robust against the aforementioned parametric uncertainties and operating point variation is proposed. A robust control approach is selected owing to the systematic design approach, fixed-order controller, and suitability for industrial applications.

A. Controller Synthesis

The employed structure is a controller with a single DOF, and both reference tracking and disturbance rejection are simultaneously guaranteed. Thus, the controller is synthesized based on the internal model principle to guarantee both reference tracking and disturbance rejection of step signals at the input and output, respectively [25]. The applied control structure is depicted in Fig. 6.

One of the best ways to optimally reject the disturbance signal affecting the output is to minimize the H_∞ norm from the filtered disturbance signals to the filtered output in the presence of weighted uncertainty using the structured singular values (μ) analysis by applying the *DK*-iteration method. Therefore, a μ-synthesis controller using the *DK*-iteration method is employed to optimally synthesize the controller [26]–[30].

It is worth noting that although the polynomial method can be employed for robust dc-link voltage control [9], it is not applicable in the problem addressed in this paper. This is because the range of variation of vertices of the polytopic system proposed in [28] is so vast that the linear matrix inequality condition is not feasible [9], [28], [29].

In order to have one structure that models changeable variables discussed in Section III, all possible transfer functions have been randomly generated by MATLAB. The uncertain plant model given by (26) contains six uncertain elements—*A*, *B*, *E*, *a*, *b*, and *e*—that are affected by I_{d-0}, I_{q-0}, $L_{\rm DC-eq}$, and

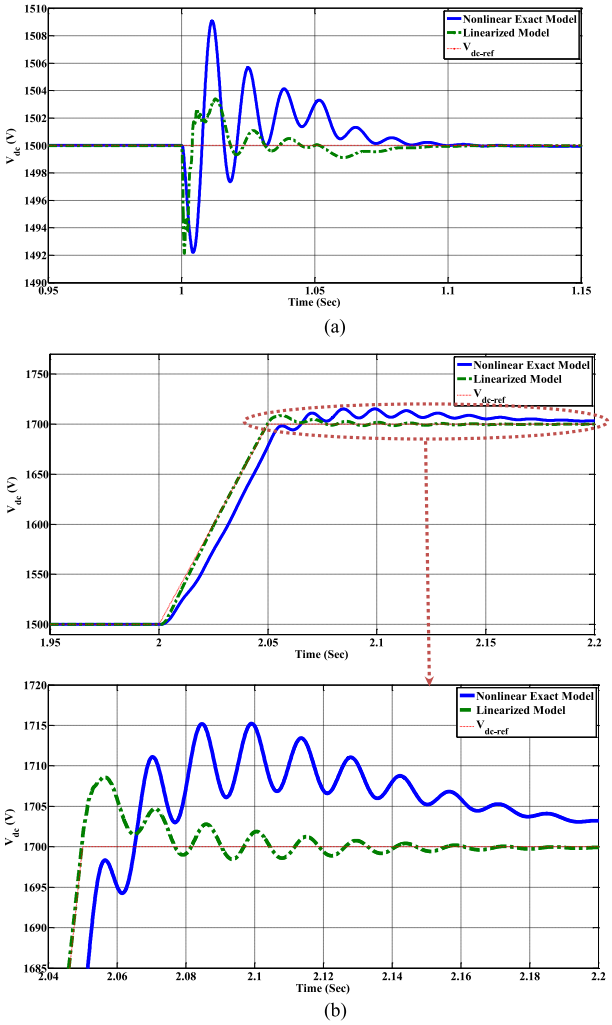

Fig. 7. Results of model validation for the inversion mode. (a) V_{dc} for the nonlinear and linearized model when 0.25 MW is loaded on the converter working at +2.25/0.00 MW/MVAr. (b) V_{dc} and $V_{\mathrm{dc-ref}}$ for the nonlinear and linearized model when $V_{\mathrm{dc-ref}}$ is changed from 1500 to 1700 V.

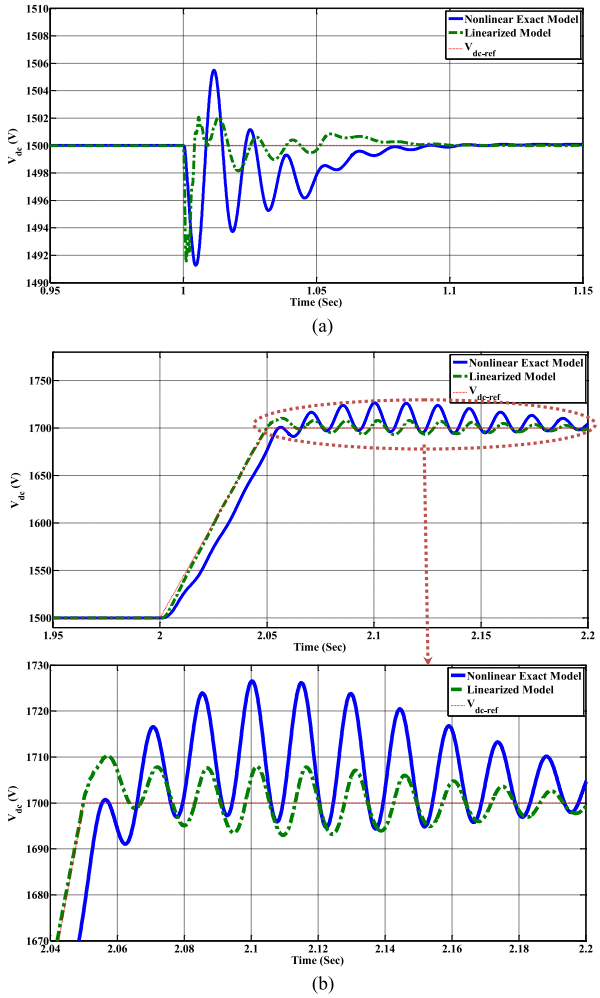

Fig. 8. Results of model validation for the rectification mode. (a) V_{dc} for the nonlinear and linearized model when 0.25 MW is loaded on the converter working at –2.25/0.00 (MW/MVar). (b) V_{dc} and $V_{\mathrm{dc-ref}}$ for the nonlinear and linearized model when $V_{\mathrm{dc-ref}}$ is changed from 1500 to 1700 V.

C_{eq}. It is often appropriate to simplify the uncertainty model while approximately retaining its overall variability for optimal feedback design purposes. One hundred twenty random samples of all possible transfer functions have been generated, and the nominal transfer function and its related unmodeled dynamics have been extracted using the MATLAB Robust Control Toolbox [19]. Referring to Fig. 9 and using the nominal system parameters, the transfer functions $G(s)$ and $W(s)$ are given by

$$G(s) = \frac{-649.5s^2 - 5.641 \times 10^{-8}s - 1.748 \times 10^{+9}}{s^3+353.8s^2+1.785 \times 10^{+5}s+2.956 \times 10^{+7}} \quad (36)$$

$$W(s) = \frac{1.732s^2 + 1224s+3.062 \times 10^{+4}}{s^2+347.5s+1.552 \times 10^{+4}}. \quad (37)$$

Also, the designed transfer functions $W_d(s)$ and $W_p(s)$ are given by

$$\mathrm{W}_d(\mathrm{s}) = \frac{1}{s+10^{-4}} \quad (38)$$

$$\mathrm{W}_p(\mathrm{s}) = \frac{1}{s+10^{-3}}. \quad (39)$$

$$K(s) = \frac{-0.0007032s^7 - 0.07585s^6 - 0.08029s^5 - 0.0163s^4 - 0.0009548s^3 - 9.625 \times 10^{-7}s^2 - 2.879 \times 10^{-10}s - 2.098 \times 10^{-14}}{s^7 + 0.284s^6 + 0.01924s^5+3.708 \times 10^{-5}s^4 + 2.433 \times 10^{-8}s^3 + 6.286 \times 10^{-12}s^2 + 5.087 \times 10^{-16}s + 3.159 \times 10^{-21}} \quad (40)$$

By choosing *G(s)* as the nominal plant dynamics, the controller guarantees robust performance and stability with varying *A*, *B*, *E*, *a*, *b*, and *e*. $W_d(s)$ is selected using (38) to reject $P_{\rm ext}$ as much as possible by minimizing the H_∞ norm from disturbance to the output in Fig. 9. $W_p(s)$ is selected using (39) to induce internal model dynamics and, hence, facilitates simple controller design with appropriate performance [25], [30].

The controller *K*(*s*) given by (40), shown at bottom of the previous page. Has been synthesized using the robust controller design approach via the μ-synthesis and model order reduction tools in the Robust Control Toolbox of MATLAB.

As shown in Fig. 6, the synthesized controller is a single transfer function employed in the 1-DOF structure, which simplifies the implementation. In spite of the somewhat high controller order, it is relatively easy to implement using commercial-grade signal processors.

B. Model Validation

The robust controller designed in Section IV-A is employed for two different transfer functions generated by (26) for two modes of rectification and inversion operating close to maximum VSC capacity. The same controller is then employed with the total nonlinear system, and the results are obtained at the same operating points used for linearization. Six scenarios have been considered—three for the inversion mode and three for the rectification mode. For the inversion mode, the VSC works at +2.25/0.00 MW/MVAr; an additional 0.25 MW is then loaded on the converter. The corresponding transfer function is extracted from (26) for the operating point +2.25/0.00 MW/MVAr. The reference dc-link voltage $V_{\rm DC-ref}$ is then set to increase to 1700 V, while the VSC works at 2.5/0.00 MW/MVAr for both cases. For the rectification mode, the VSC works at –2.25/0.00 MW/MVAr; an additional 0.25 MW is then loaded on the converter. The corresponding transfer function is extracted from (26) for the operating point –2.25/0.00 MW/MVAr. $V_{\rm DC-ref}$ is then set to increase to 1700 V, while the VSC works at −2.5/0.00 MW/MVAr for both cases. The obtained results are compared and demonstrated in Figs. 7 and 8.

Figs. 7 and 8 demonstrate acceptable compatibility between the closed-loop response of the nonlinear plant and the linearized model extracted from the nonlinear plant working at the appropriate operating point. In fact, the number and instant of occurrence of the oscillations are very well matched and consistent for both responses of the nonlinear and linearized plants. The results reveal the validity of the linearized model for which the LTI robust controller was designed. Close matching is observed at different values of operating points and nominal dc-link voltages.

V. Simulation Results

A typical multiterminal dc grid with four terminals, presented in Fig. 9, was considered for the simulation study to test the performance of the proposed control system under typical and practical disturbances imposed under multiconverter operation in modern dc grids. The system was simulated in the MATLAB/Simulink environment. The system was composed of four zones. Zone I was a 580 V, 60 Hz ac grid that can inject or absorb power to or from the point of common coupling (PCC-1). Zone I mimicked the grid-connected VSC. Zone II was a 580 V 60 Hz grid interfaced to the dc side of Zone I via a VSC to control the power flow from or to PCC-2. The VSC in Zone II, VSC-PQ, was controlled in the PQ mode. Zone III was composed of a 1.0-MW renewable energy source that could produce dc power (e.g., full-scale wind turbine system). A VSC, VSC-W, was used to interface the variable-frequency wind turbine system to the dc grid. Zone IV modeled a 1.0-MW 500-$V_{\rm dc}$ dc microgrid with energy storage system (ESS) interfaced to the dc grid via a bidirectional dc/dc converter. The controllers employed in different zones are shown in Fig. 2. In Zone I, the VSC worked as a dc voltage power port to control the dc-link voltage. Zone II employed a standard voltage-oriented PQ control structure with inner PI current control loops in the synchronous *dq*-frame [11]. Zone III employed a synchronous-frame PI controller applied in *dq*-frame. Zone IV employed a standard PI controller for the bidirectional dc/dc converter. The complete system parameters are given in Appendix II. The proposed controller was applied to the VSC in Zone I using the system parameters given in Appendix II.

The average model of VSCs in Zones I, II, and III is used to reduce the computational burden without loss of accuracy. A switching model of the bidirectional dc/dc converter system (Zone IV) was implemented to test the control performance under typical high-frequency disturbances associated with converter switching. To evaluate and demonstrate the performance of the proposed voltage control scheme, the proposed controller was tested as follows; key results are reported accordingly.

First, the dc-side capacitor was energized from its initial zero state by a ramp function that started from zero at $t = 0$ and increased to its final value, 1500 V, at $t = 0.05$ s. Zone II was then connected to the dc grid at $t = 0.10$ s with zero active and reactive power. At $t = 1.00$ s, Zone II was set to absorb 2.25 MW/2.0 VAr from the dc grid and inject to its ac grid; the reactive power command of Zone II was kept constant within the rest of the simulation. Thus, the grid-connected VSC worked as a rectifier, and it injected 2.25-MW/0.00 VAr active/reactive power to its ac grid. At $t = 2.00$ s, Zone II was set to inject 2.0 MW to the dc grid, so it absorbed 2.0 MW from its ac grid; meanwhile, it still injected 2.0 MVAr to its ac grid. Thus, the grid-connected VSC worked as an inverter, and it absorbed 2.0 MW from the dc grid. Also, Zone I was set to inject 1.00 MVAr to its ac grid at $t = 2.5$ s; the reactive power command of Zone I was kept constant within the rest of the simulation. Zone II was again set to absorb 2.0 MW from the dc grid and inject to its ac grid at $t = 3.00$ s; again, within this period, it still injected 2.0 MVAr to its ac grid. This situation was kept for Zone II during the rest of the simulation.

Afterward, Zone III, which mimicked a wind farm directly connected to the dc grid via a single VSC, was connected to the dc grid at $t = 4.00$ s. It injected 2.0 MW into the dc grid at unity power factor, and it reduced its power from 2.0 to 0.0 MW during the period from $t = 4.50$ s to $t = 4.55$ s.

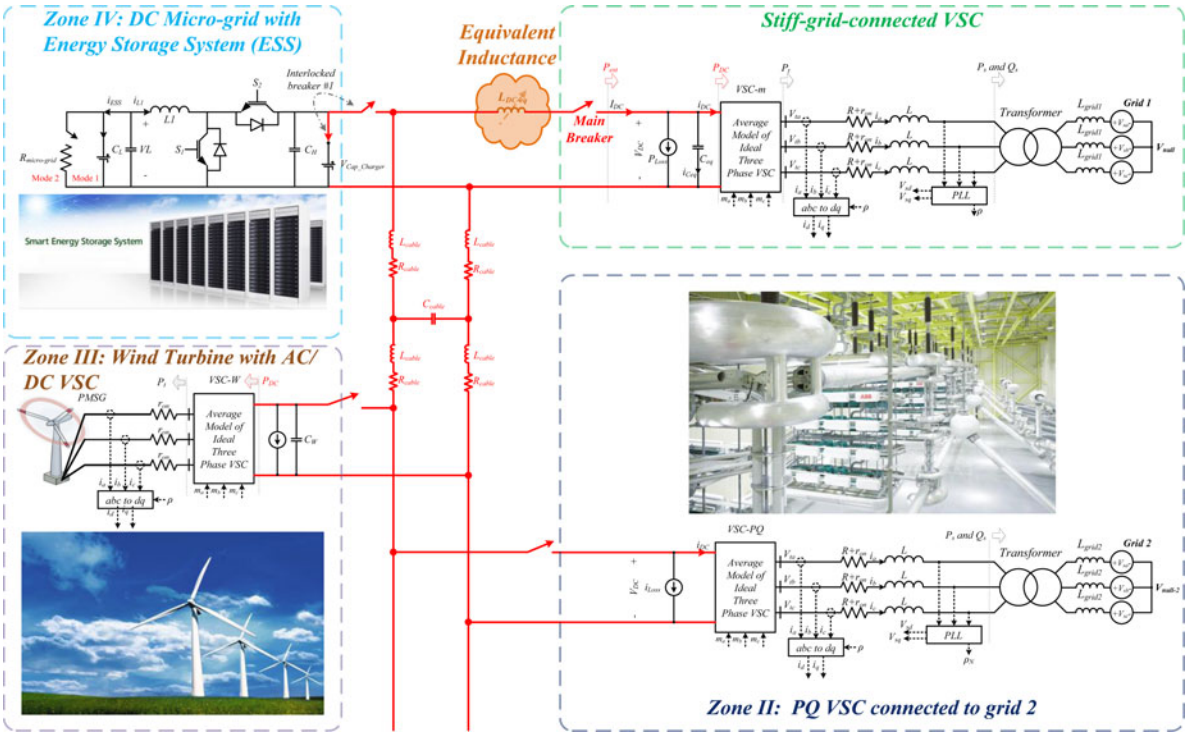

Fig. 9. Detailed structure of the simulated network.

Finally, Zone IV was connected to the dc grid at $t = 5.0$ s using interlocked breaker #1. Initially, the dc microgrid load was disconnected, and the ESS was controlled in the boost mode to inject 0.75 MW to the dc grid by controlling the inductor current i_{L1} in Fig. 1 via a simple PI controller. The dc microgrid load was connected to the bidirectional dc/dc converter, and the battery was disconnected to model a contingency event and test the performance of the proposed controller under overload conditions. Accordingly, the dc/dc converter was set to suddenly change its control mode from boost to buck in order to transfer 0.90 MW from the dc grid to the dc microgrid load. The power reversal instant was at 5.50 s, and it lasted approximately 0.70 s.

To assess the system performance under a static load connection to the dc grid, a 1.00-MW dc static load, which is equivalent to 2.25 Ω at 1500 V, was directly connected to the dc grid without any interface at $t = 4.2$ s, and then it was directly disconnected from the dc grid at $t = 4.7$ s.

The control performance of the proposed controller under various simulation scenarios is shown in Figs. 10–12. The figures show the performance of the stiff-grid-connected VSC (connected to Grid1) under several scenarios of injecting and absorbing power into and from the dc network. Despite the large power disturbance and the uncertainty in the equivalent dc-link capacitor as "seen" by the VSC owing to the connection of VSC-PQ and the wind-turbine VSC with local dc-link capacitor of 3000 μF, robust voltage control performance was yielded with over-/undershoot voltage that was less than 30 V (2.00%) and recovery time of approximately 0.2 s.

Furthermore, the controller performance when connecting/disconnecting the dc static load is shown in Fig. 10; the

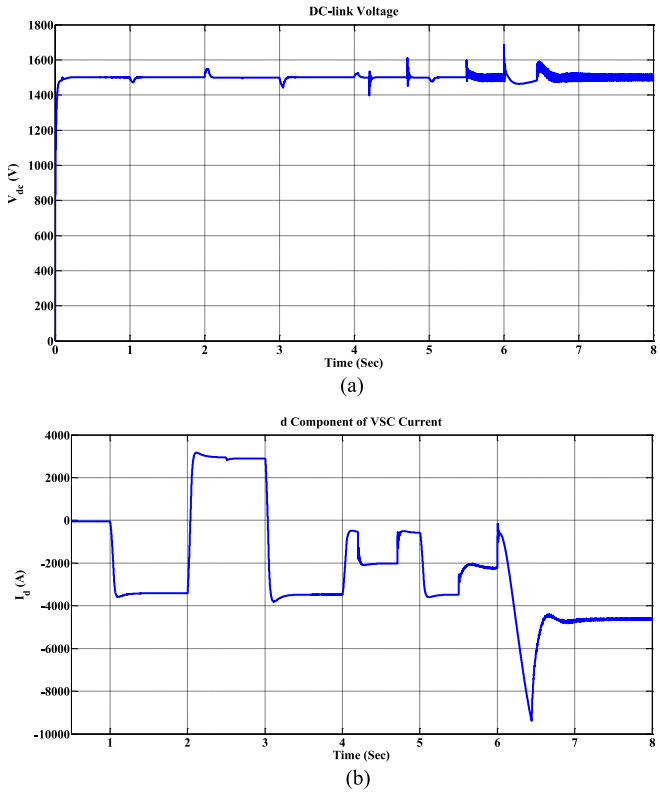

Fig. 10. Simulation results: (a) DC-link voltage of the VSC in Zone 1. (b) I_d of the VSC in Zone 1.

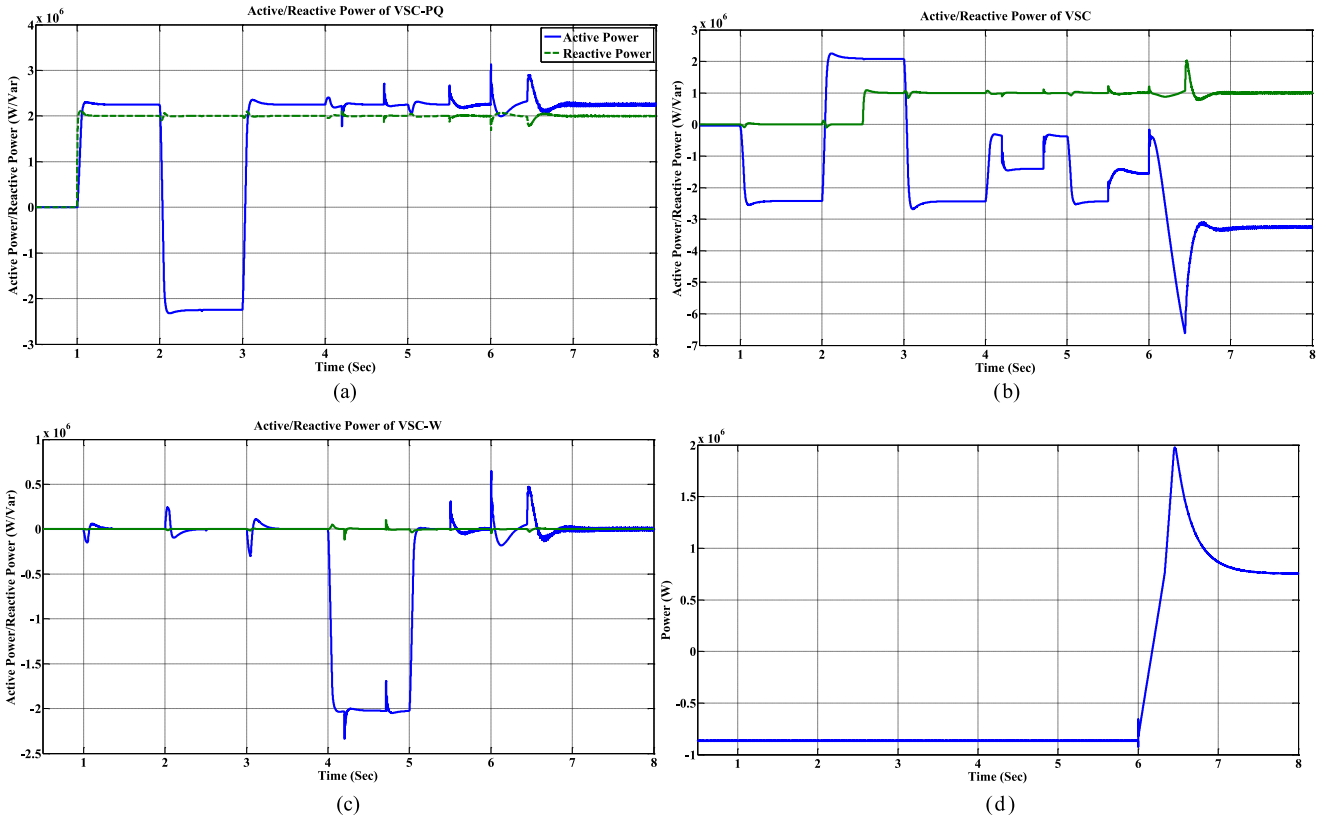

Fig. 11. Active and reactive power responses in different zones of Fig. 9. (a) Active-reactive power of VSC-PQ. (b) Active-reactive power of the grid-connected VSC. (c) Active-reactive power of VSC-W. (d) Active power of the ESS.

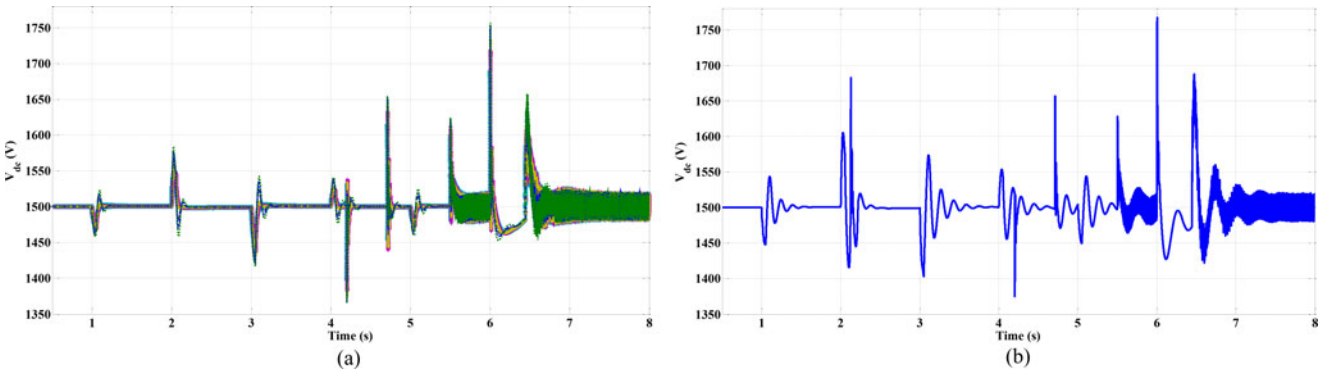

Fig. 12. Performance of the proposed controller under changes in the value of $L_{\mathrm{DC-eq}}$. (a) $L_{\mathrm{DC-eq}} = 3000\ \mu$H, i.e., within a specific range for which the controller synthesized, $0 < L_{\mathrm{DC-eq}} < 4500\ \mu$H, (b) out of the specific range for which the controller synthesized, $L_{\mathrm{DC-eq}} = 7500\ \mu$H.

maximum over-/undershoot voltage (for average dc voltage) is 115/103 V (7.67%/6.87%) with a recovery time of 0.05 s.

In addition, Fig. 11 shows the controller performance when the ESS was connected via a bidirectional dc/dc converter. Again, in spite of the harsh transient conditions—i.e., I_d changes from approximately 0 A to approximately –9000 A, which drifts the operating point outside the rated power range (approximately 2.57 per unit where the nominal value of I_d is approximately $\pm$3524 A) to challenge the controller's performance, the maximum over-/undershoot voltage (for average dc, not switching, voltage) is 150/40 V (10%/2.66%) with a recovery time of 0.1 s. The proposed controller successfully ensures robust voltage control performance in the presence of dynamic interactions between the dc/dc converter and the dc grid and in operating points outside the range used for the controller design.

This section has been allocated to compare the performance of the proposed controller with another recently developed robust dc-link voltage controller [9]; the suggested controller in [9] has been employed in the comparative study because it improves the dc-link voltage performance compared to that of the PI-lead controller [12]. Furthermore, it was designed considering the instantaneous power of the ac-side inductor; therefore,

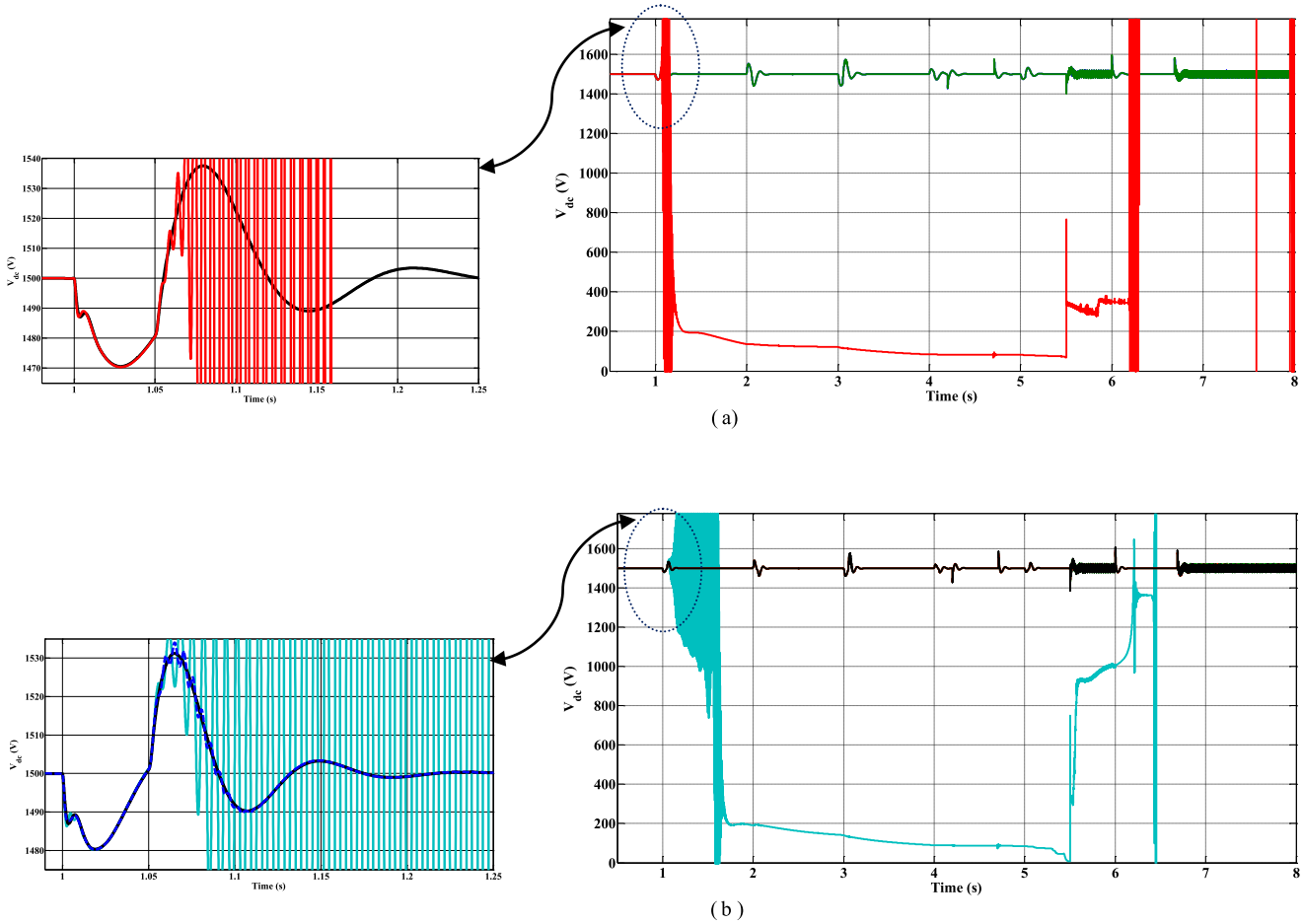

Fig. 13. Performance of the controller in [9] under uncertainty in $L_{\rm dc}$. $L_{\rm DC-eq} = 300$ μH: (a) with the full controller synthesized in [9], (b) with the controller synthesized by means of the first step in [9].

it is a good candidate to verify the unique impact of the instantaneous power of the dc inductor. Consequently, the proposed controller and the controller reported in [9] were simulated for different values of the dc inductor. The simulation results are shown in Figs. 12 and 13. Both controllers were tested under the simulation parameters described previously.

As predicted by the theoretical analysis, the proposed controller demonstrated sufficient robustness against changes in the value of $L_{\rm DC}$ within a specific range. One simulation was conducted for $L_{\rm DC-eq} = 7500$ μH, which is out of the specific range ($0 < L_{\rm DC-eq} < 4500$ μH) used to design the robust controller to further challenge the proposed controller. The dc-link voltage remains stable as shown in Fig. 12. However, the closed-loop system was not stable, even with the nominal value of $L_{\rm DC}$, when the controller synthesized by the method suggested in [9] was employed to stabilize the dc-link voltage. It is worth noting that the controller proposed in [9] contained two steps for the purpose of synthesizing a robust dc-link voltage controller. In the first step, the controller was robust only against operating point variations induced by the instantaneous power changes of the three-phase ac-side inductor L. In the second step, the controller was altered to ensure robustness against $C_{\rm eq}$ variation and have all closed-loop poles within a prespecified region in the s-plane. Although $C_{\rm eq}$ was fixed to its nominal value to nullify the effect of $C_{\rm eq}$ changes in the simulation results demonstrated in Fig. 13, both controllers failed to stabilize the dc-link voltage dynamics when the nominal value of $L_{\rm DC}$ was employed.

VI. Experimental Results

For further evaluation of the proposed controller, a laboratory-scale experimental test system, depicted in Fig. 14, was employed to emulate the performance of a high-power grid-connected VSC with an *LC* filter at the dc side in a typical dc grid. The experimental system consisted of a grid-connected VSC and dc-side static and dynamic loads modeling a dc microgrid. The VSC was controlled in the rectification mode, which yielded the worst-operating conditions with respect to dc-link voltage stability. A Semistack intelligent power module—which included gate drives, six insulated gate bipolar transistors, and a protection circuit—was used to implement the grid-connected VSC. The switching frequency was 10 kHz. The ac-side filter inductance and resistance were 2.4 mH and 0.06 Ω, respectively. The dc-link capacitance and inductance were 2.04 mF and 1.70 mH, respectively. The VSC was rated at 35 A, 380 V. However, the VSC was not operated at the rated power in order to emulate high-power converter dynamics in the experimental setup

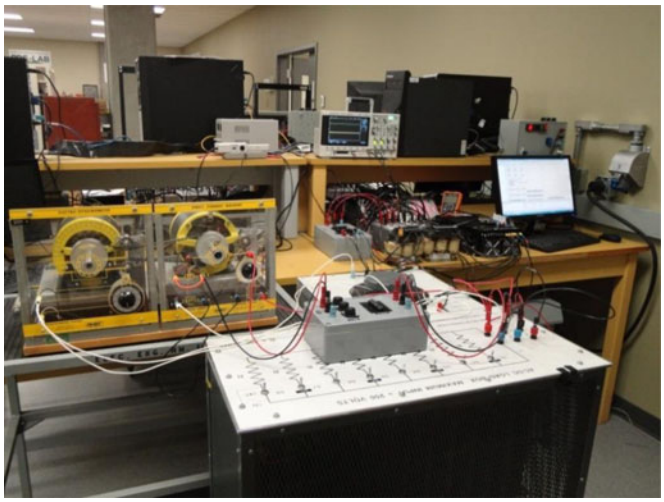

Fig. 14. View of the experimental setup.

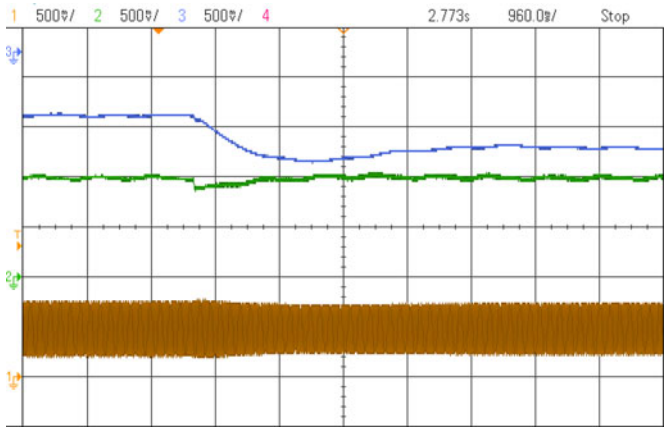

Fig. 15. Experimental results of the proposed controller performance under connected static dc load and existing uncertainty in the components of dc-link filter, dc side capacitor and inductor, as well as operating point variations; Channel 3 (top line): control lever, i_d, the positive value is considered when the power is flowing from the dc side to the ac side 10 A/Div; Channel 2 (middle line): $V_{\rm dc}$ in per unit, 0.5 V/Div; Channel 1 (bottom line): modulation index of phase A (bounded between 0 and 1 based on dSPACE1104 requirements), 0.5 V/Div; horizontal axis: 960 ms/Div.

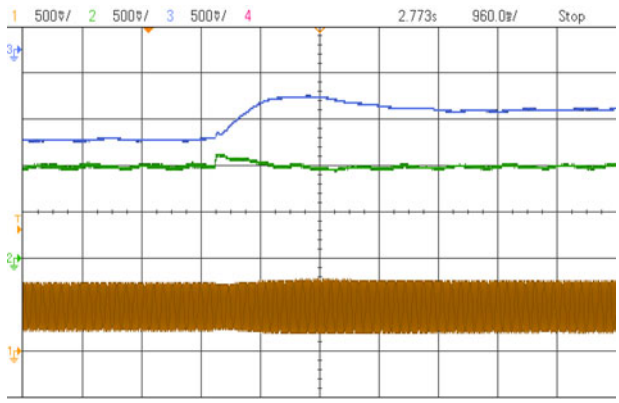

Fig. 16. Experimental results of the proposed controller performance under disconnected static dc load and existing uncertainty in the components of dc-link filter, dc side capacitor and inductor, as well as operating point variations; Channel 3 (top line): control lever, i_d, the positive value is considered when the power is flowing from the dc side to the ac side 10 A/Div; Channel 2 (middle line): $V_{\rm dc}$ in per unit, 0.5 V/Div; Channel 1 (bottom line): modulation index of phase A (bounded between 0 and 1 based on dSPACE1104 requirements). 0.5 V/Div; horizontal axis: 960 ms/Div.

[10]. Consequently, the laboratory-scale converter is derated to 1.00 kW, 30 V, 25 A.

The VSC inductor currents were measured by HASS-50-S current sensors, and the voltages were measured by LEM-V-25-400 voltage sensors. The converter was interfaced with a dSPACE1104 control card by means of a CMOS/TTL interfacing circuit. PWM modulations and the proposed dc-link controller were implemented on the dSPACE1104 control card supported with a TMS320F240-DSP coprocessor structure for switching signal generation. The dSPACE1104 interfacing board was equipped with eight digital-to-analog channels and eight analog-to-digital channels to interface the measured signals to/from the control system. The software code was generated by the Real-Time Workshop in a MATLAB/Simulink environment. The dc-side load was composed of an *LC* filter connected to a resistive load box and a dynamic load, which could be used as an effective means to model a dc microgrid with both static and dynamic loads. The dynamic load was composed of a Lab-Volt DC motor loaded by a dynamometer.

The proposed controller was tested under the rectification mode when connecting/disconnecting different types of dc loads to/from the dc grid. The impact of both a static load and a dynamic load on dc grid dynamics was considered in the experimental test. Also, the effective dc-link capacitance was doubled to assess the robustness of the proposed controller against variation in the effective dc-link capacitance.

Fig. 15 shows the performance of the proposed dc-link voltage control under parametric uncertainty and operating point variation. The actual dc-link capacitance was doubled, whereas the nominal value was used in the controller design. Further, the dc-side inductance was doubled, and the static load was suddenly connected to generate variation in the operating point (from no load to full load) and excite the system dynamics. Fig. 16 shows the system performance under the same conditions with load disconnection. The first trace in Figs. 15 and 16 shows the control level and the direct-axis current, the second trace shows the dc-link voltage, and the third trace shows the corresponding modulation index for phase A.

Additionally, Figs. 17 and 18 depict the performance of the proposed controller under connection/disconnection of the active load (DC motor) to/from the dc grid. The dynamic load generated continuous variation in the operating point along with the added parametric uncertainties. The proposed controller maintained robust performance under operating point variation and parametric uncertainties. Furthermore, the voltage over-/undershoot and recovery times were very small, which ensured perfect regulation performance.

Fig. 19 shows the performance of the robust controller in [9] when the dc-link inductor was added and removed. Because the controller was designed without considering any uncertainty in the dc-link inductance, the system became unstable when the

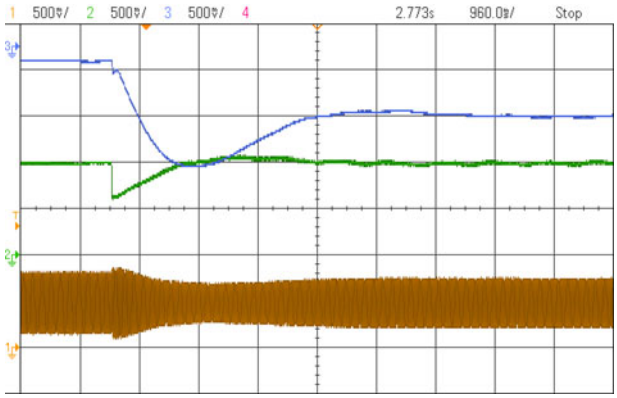

Fig. 17. Experimental results of the proposed controller performance under connected active dc machine load and existing uncertainty in the components of dc-link filter, dc side capacitor and inductor, as well as operating point variations; Channel 3 (top line): control lever, i_d, the positive value is considered when the power is flowing from the dc side to the ac side 10A/Div; Channel 2 (middle line): $V_{\rm dc}$ in per unit, 0.5 V/Div; Channel 1 (bottom line): modulation index of phase A (bounded between 0 and 1 based on dSPACE1104 requirements). 0.5 V/Div; horizontal axis: 960 ms/Div.

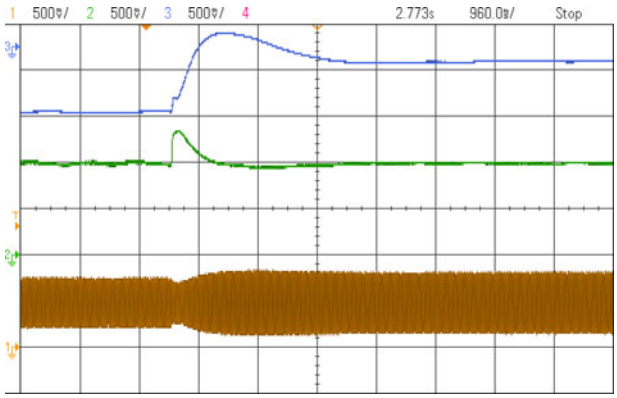

Fig. 18. Experimental results of the proposed controller performance under connected active dc machine load and existing uncertainty in the components of dc-link filter, dc side capacitor and inductor, as well as operating point variations; Channel 3 (top line): control lever, i_d, the positive value is considered when the power is flowing from the dc side to the ac side 10 A/Div; Channel 2 (middle line): $V_{\rm dc}$ in per unit, 0.5 V/Div; Channel 1 (bottom line): modulation index of phase A (bounded between 0 and 1 based on dSPACE1104 requirements). 0.5 V/Div; horizontal axis: 960 ms/Div.

physical dc-link inductance was added. Stability was regained when the dc-link inductance was bypassed. Therefore, even with a robust dc-link voltage controller, the effect of the dc-side inductance could destabilize the system. Therefore, accurate modeling is needed to design an effective robust controller.

VII. Conclusion

Dynamics and control of VSCs considering the instantaneous power of both the ac-side filter and uncertain dc-side inductor have been addressed in this paper. Uncertainty in the dc-side component parameters, including filter capacitance and dc-side inductance, affects the stability and performance of the converter owing to connecting/disconnecting electric devices to/from the dc grid. Furthermore, small-signal dynamic analysis has shown

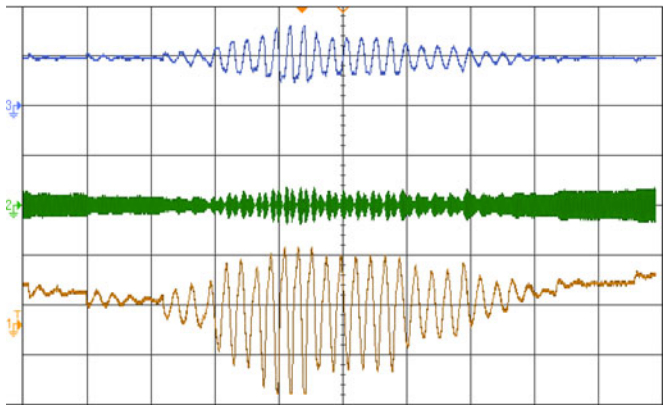

Fig. 19. Experimental results of the controller in [9] under connection/disconnection of dc-side inductor uncertainty. Channel 3 (top line): $V_{\rm dc}$ in per unit, 0.5 V/Div. Channel 2 (modulation index of phase A [bounded between 0 and 1 based on dSPACE1104 requirements]. 0.5 V/Div), Channel 1 (third line) control lever, i_d.

that the dc-link voltage dynamics are highly dependent on the converter operating point. When operating point variation is combined with possible parametric uncertainties, unstable open-loop dynamics along with nonminimum phase behavior can be easily generated in grid-connected converters. To overcome those difficulties, this paper has presented a detailed small-signal model of the dc-link dynamics in grid-connected VSCs while the instantaneous power of both ac- and dc-side energy storage components are considered, and then a robust optimal dc-link voltage controller is designed. The proposed controller has yielded excellent tracking performance, robust disturbance rejection, and robust performance against operating point and parameter variation with a simple fixed-parameter controller. Comparative simulation studies and experimental results have validated the theoretical results and demonstrated the effectiveness of the proposed control structure.

Appendix I

Parameters of the system shown in Fig. 1:

Stiff-grid-connected VSC: Rated power = 2.5 MVA; Grid 1 voltage = 580 V at 60 Hz; $P_{\rm Loss} = 5000$ W; $R = 1.5$ mΩ; $L = 300$ μH; switch resistance = 1.0 mΩ; diode resistance = 1.0 mΩ; $K_p = 0.3$ Ω; $K_i = 3.5$ Ω/s; $R_{\rm res} = 1\Omega$; uncertain parameters: dc filter capacitor: 6250 μF $< C_{\rm eq} <$ 18 500 μF; 0 μH $< L_{\rm DC-eq} <$ 4500 μH; 1.125 $\Omega < R_{\rm L} <$ 250.

DC grid: Rated voltage = 1500 V, dc cable length = 50 km, $R_{\rm cable} = 0.82$ mΩ/km, $C_{\rm cable} = 0.014$ μF/km, $L_{\rm cable} = 0.98$ μH/km.

Appendix II

Parameters of the system shown in Fig. 9:

DC grid: Rated voltage = 1500 V, dc cable length = 50 km, $R_{\rm cable} = 0.82$ mΩ/km, $C_{\rm cable} = 0.014$ μF/km, and $L_{\rm cable} = 0.98$ μH/km.

DC Filter: $C_f = 3000$ μF, $L_{\rm DC-eq} = 300$ μH, and $R_{\rm res} = 1$ Ω.

Zone I: Grid-connected VSC: VSC-PQ: rated power = 2.5 MVA, grid 2 voltage = 580 V at 60 Hz; $P_{\rm Loss} = 5000$ W; $R = 0.06$ mΩ; $L = 300$ μH; switch resistance = 1.0 mΩ; diode resistance = 1.0 mΩ; $K_p = 0.06\Omega$; $K_i = 0.7\Omega$/s.

Zone II: VSC-PQ: rated power = 2.5 MVA, grid 2 voltage = 580 V at 60 Hz; $P_{\rm Loss} = 5000$ W; $R = 0.06$ mΩ; $L = 300$ μH; $C = 3000$ μF, switch resistance = 1.0 mΩ; diode resistance = 1.0 mΩ; $K_p = 0.06\Omega$; $K_i = 0.7\Omega$/s.

Zone III VSC-W: rated power = 2.5 MVA, grid 2 voltage = 580 V at 60 Hz; $P_{\rm Loss} = 5000$ W; $R = 0.06$ mΩ; $L = 300$ μH; $C = 3000$ μF, switch resistance = 1.0 mΩ; diode resistance = 1.0 mΩ; $K_p = 0.06\Omega$; $K_i = 0.7\Omega$/s.

Zone IV: power rating = 0.9 MW, ESS and load voltage: 500 $\rm V_{dc}$, $C_L = 1000$ μF, $C_H = 6000$ μF, $L_1 = 100$ mH, $R_{\rm DC} = 1\,\Omega$, $K_{\rm p}$ (mode1) = 0.4, $K_{\rm i}$ (mode1) = 4×10^{-4}, $K_{\rm p}$ (mode2) = 0.0133, $K_{\rm i}$ (mode2) = 0.0533, $V_{L\_\rm Ref} = 500$ V, $i_{L\_\rm Ref} = 1800$ A.

REFERENCES

[1] U.S. Department of Energy. *The War of the Currents: AC Vs. DC Power*. (2014, Nov. 18). [Online]. Available: http:// energy.gov/articles/war-currents-ac-vs-dc-power.

[2] R. Rudervall, J. P. Charpentier, and R. Sharma, "High voltage direct current (HVDC) transmission systems technology review paper," presented at the Energy Week 2000, Washington, DC, USA, Mar. 7/8, 2000.

[3] N. G. Hingorani, "High voltage DC transmission: A power electronics workhorse," *IEEE Spectr.*, vol. 33, no. 4, pp. 63–72, Apr. 1996.

[4] P. Wang, L. Goel, X. Liu, and F. H. Choo, "Harmonizing AC and DC: A hybrid AC/DC future grid solution," *IEEE Power and Energy Mag.*, vol. 11, no. 3, pp. 76–83, Apr. 2013.

[5] P. Fairley, "Germany jump-starts the supergrid," *IEEE Spectr.*, vol. 50, no. 5, pp. 36–41, May 2013.

[6] X. Liu, P. Wang, and P. C. Loh, "A hybrid AC/DC microgrid and its coordination control," *IEEE Trans. Smart Grids*, vol. 2, no. 2, pp. 278–286, Jun. 2012.

[7] D. Chen and L. Xu, "Autonomous DC voltage control of a DC microgrid with multiple slack terminals," *IEEE Trans. Power Syst.*, vol. 27, no. 4, pp. 1897–1905, Nov. 2012.

[8] A. Radwan and Y. A.-R. I. Mohamed, "Assessment and mitigation of interaction dynamics in hybrid AC/DC distributed generation networks," *IEEE Trans. Smart Grids*, vol. 3, no. 3, pp. 1382–1393, 2012.

[9] M. Davari and Y. A.-R. I. Mohamed, "Robust multi-objective control of VSC-based DC-voltage power port in hybrid AC/DC multi-terminal microgrids," *IEEE Trans. Smart Grids*, vol. 4, no. 3, pp. 1597–1612, Sep. 2013.

[10] M. Davari and Y. A.-R. I. Mohamed, "Variable-structure-based nonlinear control for the master VSC in DC-energy-pool multiterminal grids," *IEEE Trans. Power Electron.*, vol. 29, no. 11, pp. 6196–6213, Nov. 2014.

[11] M. P. Kazmierkowski and L. Malesani, "Current control techniques for three-phase voltage-source PWM converters: A survey," *IEEE Trans. Ind. Electron.*, vol. 45, no. 5, pp. 691–703, Oct. 1998.

[12] A. Yazdani and R. Iravani, *Voltage-Sourced Converters in Power Systems*, 1st ed. Hoboken, NJ, USA: Wiley, 2010.

[13] C. Gavriluta, J. I. Candela, J. Rocabert, A. Luna, and P. Rodriguez, "Adaptive droop for control of multiterminal dc bus integrating energy storage," *IEEE Trans. Power Del.*, vol. 30, no. 1, pp. 16–24, Feb. 2015.

[14] T. Luth, M. M. C. Merlin, T. C. Green, F. Hassan, and C. D. Barker, "High-frequency operation of a dc/ac/dc system for HVDC applications," *IEEE Trans. Power Electron.*, vol. 29, no. 8, pp. 4107–4115, Aug. 2014.

[15] T. B. Soeiro, F. Vancu, and J. W. Kolar, "Hybrid active third-harmonic current injection mains interface concept for dc distribution systems," *IEEE Trans. Power Electron.*, vol. 28, no. 1, pp. 7–13, Jan. 2013.

[16] Z.-D. Wang, *et al.* "A coordination control strategy of voltage source converter based MTDC for offshore wind farms," *IEEE Trans. Ind. Appl.*, to be published, doi: 10.1109/TIA.2015.2407325.

[17] K. Rouzbehi, A. Miranian, J. I. Candela, A. Luna, and P. A Rodriguez, "Generalized voltage droop strategy for control of multiterminal dc grids," *IEEE Trans. Ind. Appl.*, vol. 51, no. 1, pp. 607–618, Jan./Feb. 2015.

[18] E. Kontos, R. T. Pinto, S. Rodrigues, and P. Bauer, "Impact of HVDC transmission system topology on multiterminal dc network faults," *IEEE Trans. Power Del.*, vol. 30, no. 2, pp. 844–852, Apr. 2015.

[19] Q. Mu, J. Liang, X. Zhou, Y. Li, and X. Zhang, "Improved ADC model of voltage-source converters in dc grids," *IEEE Trans. Power Electron.*, vol. 29, no. 11, pp. 5738–5748, Nov. 2014.

[20] (2012, Sep.). *1321 Power Conditioning Products*, Publication 1321-TD001O-EN-P, Technical Data by Rockwell Automation, pp. 1–26, [Online] Available: http://literature.rockwellautomation.com/idc/groups/literature/documents/td/1321-td001_-en-p.pdf

[21] J. Dai, S. W. Nam, M. Pande, and G. Esmaeili, "Medium voltage current source converter drives for marine propulsion system using a dual-winding synchronous machine," *IEEE Trans. Ind. Appl.*, vol. 50, no. 6, pp. 3971–3976, Nov./Dec. 2014.

[22] D. Jovcic and W. Lin, "Multiport high-power LCL DC hub for use in dc transmission grids," *IEEE Trans. Power Del.*, vol. 29, no. 2, pp. 760–768, Apr. 2014.

[23] F. Z. Peng, "Z-source inverter," *IEEE Trans. Ind. Appl.*, vol. 39, no. 2, pp. 504–510, Mar./Apr. 2003.

[24] A. A. Rockhill, M. Liserre, R. Teodorescu, and P. Rodriguez, "Grid-filter design for a multimegawatt medium-voltage voltage-source inverter," *IEEE Trans. Ind. Electron.*, vol. 58, no. 4, pp. 1205–1217, Apr. 2011.

[25] G. C. Goodwin, S. F. Graebe, and M. E. Salgado, *Control System Design*. Englewood Cliffs, NJ, USA: Prentice-Hall, 2000.

[26] K. S. Narendra and J. Balakrishnan, "Adaptive control using multiple models," *IEEE Trans. Automat. Control*, vol. 42, no. 2, pp. 171–187, Feb. 1997.

[27] D.-W. Gu, P. H. Petkov, and M. M. Konstantinov, *Robust Control Design With MATLAB*. New York, NY, USA: Springer-Verlag, 2005.

[28] D. Henrion, M. Sebek, and V. Kucera, "Positive polynomials and robust stabilization with fixed-order controllers," *IEEE Trans. Automat. Control*, vol. 48, no. 7, pp. 1178–1186, Jul. 2003.

[29] F. Yang, M. Gani, and D. Henrion, "Fixed-order robust $\rm H_{\mathbb{E}}$ controller design with regional pole assignment," *IEEE Trans. Automat. Control*, vol. 52, no. 10, pp. 1959–1963, Oct. 2007.

[30] J. C. Doyle, B. A. Francis, and A. R. Tannenbaum, "Uncertainty and Robustness," in *Feedback Control Theory*. New York, NY, USA: Macmillan, 1992, ch. 4, pp. 45–62.

Masoud Davari (S'08) was born in Isfahan, Iran, on September 14, 1985. He received the B.Sc. degree (with Hons.) in electrical engineering from the Isfahan University of Technology, Isfahan, in September 2007, and the M.Sc. degree (with Hons.) in electrical engineering from the Amirkabir University of Technology-Tehran Polytechnic, Tehran, Iran, in January 2010. He is currently working toward the Ph.D. degree with the Department of Electrical and Computer Engineering, University of Alberta, Edmonton, AB, Canada.

His research interests include dynamics and controls of power electronic converters, and modeling, analysis, and control of ac, dc, hybrid ac/dc microgrids as well as smart grids.

Mr. Davari is a Member of the Golden Key International Honour Society.

Yasser Abdel-Rady I. Mohamed (M'06–SM'011) was born in Cairo, Egypt, on November 25, 1977. He received the B.Sc. (with Hons.) and M.Sc. degrees in electrical engineering from Ain Shams University, Cairo, in 2000 and 2004, respectively, and the Ph.D. degree in electrical engineering from the University of Waterloo, Waterloo, ON, Canada, in 2008.

He is currently with the Department of Electrical and Computer Engineering, University of Alberta, Edmonton, AB, Canada, as an Associate Professor. His research interests include dynamics and controls of power converters, distributed and renewable generation, and microgrids, modeling, analysis and control of smart grids, electric machines, and motor drives.

Dr. Mohamed is an Associate Editor of the IEEE TRANSACTIONS ON INDUSTRIAL ELECTRONICS. He is also a Guest Editor of the IEEE TRANSACTIONS ON INDUSTRIAL ELECTRONICS Special Section on "Distributed Generation and Micro-Grids." He is a Registered Professional Engineer in Alberta.